nature neuroscience

Article

https://doi.org/10.1038/s41593-022-01240-0

A TREM2-activating antibody with a blood–brain barrier transport vehicle enhances microglial metabolism in Alzheimer's disease models

Received: 14 April 2022

Accepted: 29 November 2022

A list of authors and their affiliations appears at the end of the paper

Loss-of-function variants of TREM2 are associated with increased risk of Alzheimer's disease (AD), suggesting that activation of this innate immune receptor may be a useful therapeutic strategy. Here we describe a high-affinity human TREM2-activating antibody engineered with a monovalent transferrin receptor (TfR) binding site, termed antibody transport vehicle (ATV), to facilitate blood–brain barrier transcytosis. Upon peripheral delivery in mice, ATV:TREM2 showed improved brain biodistribution and enhanced signaling compared to a standard anti-TREM2 antibody. In human induced pluripotent stem cell (iPSC)-derived microglia, ATV:TREM2 induced proliferation and improved mitochondrial metabolism. Single-cell RNA sequencing and morphometry revealed that ATV:TREM2 shifted microglia to metabolically responsive states, which were distinct from those induced by amyloid pathology. In an AD mouse model, ATV:TREM2 boosted brain microglial activity and glucose metabolism. Thus, ATV:TREM2 represents a promising approach to improve microglial function and treat brain hypometabolism found in patients with AD.

Alzheimer's disease (AD) is the leading cause of dementia and represents a major global unmet medical need. Human genome-wide association studies identified numerous variants implicating microglia in modulating risk for late-onset AD (LOAD)[1,2]. Microglia are the brain's resident innate immune cells that can resolve disturbances and help maintain brain homeostasis.

A key gene modulating LOAD risk is *TREM2* (triggering receptor expressed on myeloid cells 2), encoding a lipid receptor expressed in microglia in the central nervous system (CNS)[3,4]. TREM2 signals via DAP12, an immunoreceptor tyrosine-based activating motif (ITAM) domain-containing receptor, which phosphorylates Syk for pathway activation. TREM2 is regulated by intracellular trafficking and proteolytic cleavage of the ectodomain by ADAM10/17 (refs. 5–7). TREM2 controls key microglial functions, such as phagocytosis[7,8], migration[9], lipid processing[10], proliferation, lysosomal degradation and metabolism[11]. TREM2 was shown to be required for amyloid plaque compaction in AD mouse models, myelin debris clearance in demyelinating models and neuronal health[10–14].

TREM2 coding variants significantly increase AD risk[15,16]. R47H reduces lipid ligand affinity[3,10,17,18], and H157Y abrogates signaling by increasing cell surface shedding of TREM2 (refs. 19–21). P522R is a hypermorphic variant in *PLCG2* (phospholipase C gamma 2), a downstream signaling mediator, that is protective in AD[22–25]. Finally, cerebrospinal fluid (CSF) biomarker studies indicate that higher soluble TREM2 is associated with slower AD progression[26,27]. Overall, these studies suggest that TREM2 loss of function (LOF) contributes to AD risk, and increased TREM2 function may be beneficial in AD.

Previous studies of pharmacological TREM2 activation largely report standard IgG antibodies that enter the brain via non-specific uptake due to the blood–brain barrier (BBB)[2,28–34]. Here we describe mechanisms of a novel therapeutic candidate, ATV:TREM2, a high-affinity human TREM2 antibody engineered with a monovalent

e-mail: sanchez@dnli.com; monroe@dnli.com

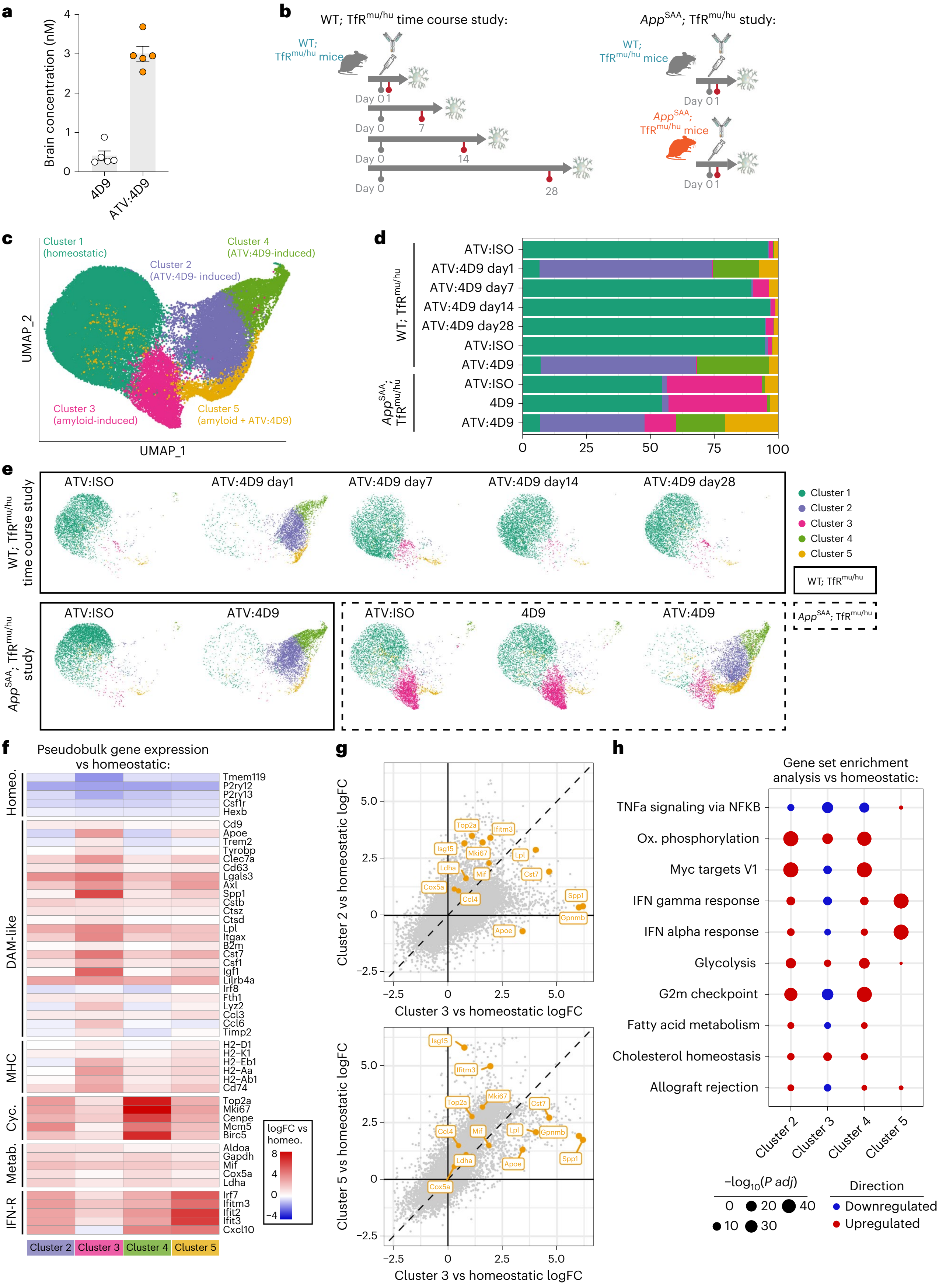
a
Brain concentration (nM)
0
1
2
3
4
4D9
ATV:4D9
b
WT; TfR$^{mu/hu}$ time course study:
WT; TfR$^{mu/hu}$ mice
Day 0 1
Day 0 7
Day 0 14
Day 0 28
App^{SAA}; TfR$^{mu/hu}$ study:
WT; TfR$^{mu/hu}$ mice
Day 0 1
App^{SAA}; TfR$^{mu/hu}$ mice
Day 0 1
c
Cluster 1 (homeostatic)
Cluster 2 (ATV:4D9- induced)
Cluster 4 (ATV:4D9-induced)
Cluster 3 (amyloid-induced)
Cluster 5 (amyloid + ATV:4D9)
UMAP_2
UMAP_1
d
WT; TfR$^{mu/hu}$
App^{SAA}; TfR$^{mu/hu}$
ATV:ISO
ATV:4D9 day1
ATV:4D9 day7
ATV:4D9 day14
ATV:4D9 day28
ATV:ISO
ATV:4D9
ATV:ISO
4D9
ATV:4D9
0
25
50
75
100
e
WT; TfR$^{mu/hu}$ time course study
ATV:ISO
ATV:4D9 day1
ATV:4D9 day7
ATV:4D9 day14
ATV:4D9 day28
App^{SAA}; TfR$^{mu/hu}$ study
ATV:ISO
ATV:4D9
ATV:ISO
4D9
ATV:4D9
● Cluster 1
● Cluster 2
● Cluster 3
● Cluster 4
● Cluster 5
WT; TfR$^{mu/hu}$
App^{SAA}; TfR$^{mu/hu}$
f
Pseudobulk gene expression vs homeostatic:
Homeo.
Tmem119
P2ry12
P2ry13
Csf1r
Hexb
DAM-like
Cd9
Apoe
Trem2
Tyrobp
Clec7a
Cd63
Lgals3
Axl
Spp1
Cstb
Ctsz
Ctsd
Lpl
Itgax
B2m
Cst7
Csf1
Igf1
Lilrb4a
Irf8
Fth1
Lyz2
Ccl3
Ccl6
Timp2
MHC
H2-D1
H2-K1
H2-Eb1
H2-Aa
H2-Ab1
Cd74
Cyc.
Top2a
Mki67
Cenpe
Mcm5
Birc5
Metab.
Aldoa
Gapdh
Mif
Cox5a
Ldha
IFN-R
Irf7
Ifitm3
Ifit2
Ifit3
Cxcl10
logFC vs homeo.
8
4
0
−4
Cluster 2
Cluster 3
Cluster 4
Cluster 5
g
Cluster 2 vs homeostatic logFC
Cluster 3 vs homeostatic logFC
−2.5
0
2.5
5.0
Top2a
Ifitm3
Isg15
Mki67
Lpl
Ldha
Mif
Cst7
Cox5a
Ccl4
Spp1
Gpnmb
Apoe
Cluster 5 vs homeostatic logFC
Cluster 3 vs homeostatic logFC
Isg15
Ifitm3
Mki67
Top2a
Cst7
Ccl4
Mif
Lpl
Gpnmb
Ldha
Apoe
Spp1
Cox5a
h
Gene set enrichment analysis vs homeostatic:
TNFa signaling via NFKB
Ox. phosphorylation
Myc targets V1
IFN gamma response
IFN alpha response
Glycolysis
G2m checkpoint
Fatty acid metabolism
Cholesterol homeostasis
Allograft rejection
Cluster 2
Cluster 3
Cluster 4
Cluster 5
−log$_{10}$(P adj)
0
10
20
30
40
Direction
● Downregulated
● Upregulated

Fig. 1 | ATV:4D9 induces temporally dynamic microglial states distinct from amyloid pathology by single-cell analysis. **a**, Antibodies were detected by human IgG ELISA in whole brain lysates 1 day after IV dose of 10 mg kg^{-1} ATV:4D9 or 4D9 (*n* = 5 mice). **b**, Designs for WT;TfR$^{mu/hu}$ and *App*^{SAA};TfR$^{mu/hu}$ studies. Mice were injected with a single IV 10 mg kg^{-1} dose of ATV:4D9 or ATV:ISO and sacrificed at indicated timepoints (*n* = 3 WT; TfR$^{mu/hu}$ mice and *n* = 4 *App*^{SAA};TfR$^{mu/hu}$ mice). **c**, Integrated UMAP projection of 49,000 total cells from all mice in both studies. The WT;TfR$^{mu/hu}$ dataset consisted of 102,043 cells, and the *App*^{SAA};TfR$^{mu/hu}$ dataset consisted of 74,758 cells (Extended Data Fig. 1a,b). Five distinct clusters of microglia were identified. **d**, Stacked bar plots of clusters distributed per group for both studies. Clusters are shown as percentages of the whole microglial compartment averaged for each biological replicate. **e**, UMAP projection split by group for cluster distribution. Data from WT; TfR$^{mu/hu}$ mice are boxed with solid lines, and data from *App*^{SAA};TfR$^{mu/hu}$ mice are boxed with dashed lines. **f**, Heat map of average log$_2$FC in each cluster compared to the 'homeostatic' cluster. Pseudobulk expression was generated by summing every counts per gene. Each mouse was treated as a biological replicate, and differential expression (DE) was performed for each cluster versus 'homeostatic' using limma. **g**, Scatter plots of the comparison of versus 'homeostatic' log$_2$FC for every gene between clusters 3 and 2 (top) and clusters 3 and 5 (bottom). In the top-right quadrant, genes falling below the dashed line are more upregulated in cluster 3, whereas genes above the dashed line are further upregulated in cluster 2 (top) or cluster 5 (bottom). Canonical DAM genes and other genes of interest are highlighted in orange. **h**, Dot plot showing GSEA for each cluster using DE versus 'homeostatic.' Signatures were taken from the hallmark gene signatures collection. Dot size is inversely proportional to log$_{10}$(corrected *P* value), and color indicates direction. No dot indicates a non-significant result. FC, fold change.

transferrin receptor (TfR) binding site in the Fc domain to enable active transport into the CNS[35]. ATV:TREM2 demonstrated improved brain exposure and CNS biodistribution compared to anti-TREM2. ATV:TREM2 promoted mitochondrial metabolic pathways, such as lipid catabolism and glucose oxidation in microglia. In AD mouse models, ATV:TREM2 induced transcription of metabolic pathway genes and increased brain glucose uptake by fluorodeoxyglucose-positron emission tomography (FDG-PET). These studies provide new insights into the mechanisms by which ATV:TREM2, a therapeutic candidate, increases microglial functions.

Results

ATV enhances brain exposure and activity of a TREM2 antibody

A mouse TREM2-specific antibody, 4D9, was previously shown to enhance protective microglial functions and reduce amyloid pathology in an AD mouse model[31]. To evaluate ATV technology, we generated ATV:4D9 on a human IgG backbone with LALA (Leu234Ala) mutations to minimize FcR binding. For in vivo studies, we employed a mouse model with the apical domain of human TfR knocked-in (TfR$^{mu/hu}$) to the mouse TfR locus, as ATV is not cross-reactive[35]. ATV:4D9 was detected at higher brain concentrations than 4D9 1 day after a 10 mg kg^{-1} intravenous (IV) dose (Fig. 1a). Capillary depletion[35–37] was used to assess BBB transcytosis. ATV:4D9 was increased in vascular and parenchymal fraction lysates (Supplementary Fig. 1a–c), which were successfully separated based on absence of endothelial markers CD31 and CLDN5 in the parenchymal fraction (Supplementary Fig. 1d). ATV:4D9 showed higher microglial co-localization compared to 4D9 by immunohistochemistry (IHC) (Supplementary Fig. 1e–h). Thus, ATV:TREM2 shows improved parenchymal delivery and targeting to microglia.

To determine if TfR binding impacts TREM2 antibody activity independently of its ability to increase brain exposure, we tested microglial responses with similar brain concentrations of ATV:4D9 and 4D9 (Supplementary Fig. 1i) and found that only ATV:4D9 significantly increased IBA1 (Supplementary Fig. 1j,k). Therefore, ATV enhances microglia responses of a TREM2 antibody despite matching brain exposures for anti-TREM2.

ATV:4D9 induces microglial states distinct from amyloid

Other groups reported that standard IgG TREM2-activating antibodies shift microglia states in vivo[32,33]. We hypothesized that ATV:TREM2 may have a broader impact on microglia via increased brain exposure. We evaluated the transcriptional dynamics of ATV:4D9 and the duration of the microglial response using single-cell RNA sequencing (scRNA-seq) over a time course after a single dose (Extended Data Fig. 1a,b) and in the context of amyloid pathology[38] (Fig. 1b and Extended Data Fig. 1a,b). Microglial state changes were highly consistent within groups (Extended Data Fig. 1c), and brain exposure was not affected by mouse genotype (Extended Data Fig. 1e).

Most microglia responded to ATV:4D9; five distinct clusters were identified after integration, uniform manifold approximation and projection (UMAP) and Louvain clustering (Fig. 1c). Most microglia were in the homeostatic cluster in isotype control-treated wild-type (WT) mice, whereas ATV:4D9 induced substantial shifts to clusters 2 and 4 after 1 day. Responsive microglial clusters largely returned to homeostasis by day 7; however, a small disease-associated microglia (DAM) cluster persisted (Fig. 1d).

ATV:4D9 increased microglial state diversity in *App*^{SAA};TfR$^{mu/hu}$ mice (Fig. 1d,e). In all four microglial clusters, responsive genes were increased compared to cluster 1. The amyloid pathology-induced cluster 3 phenocopied DAM[11,39,40] (Fig. 1f and Supplementary Table 5). The ATV:4D9-induced cluster 4 upregulated cell cycle genes and reduced expression of DAM genes compared to cluster 3 (Fig. 1f,g). Cluster 5 was induced by ATV:4D9 and amyloid pathology with upregulated IFN-stimulated genes (ISGs) with a modest upregulation of DAM genes (Fig. 1f,g).

Fig. 2 | ATV:TREM2 is a novel activating antibody that potentiates receptor clustering and endocytosis to enhance TREM2 signaling. **a**, Antibody schematic of ATV:TREM2 with human TREM2 Fab affinity and ATV binding site in the Fc domain and effectorless Fc mutations. **b**, Fluorescence polarization (FP)-based detection of TREM2 stalk peptide cleavage by recombinant ADAM17 (*n* = 4 independent experiments; two-tailed unpaired *t*-test, mean ± s.e.m.). **c**, ATV:TREM2 and PS liposome co-treatment enhanced pSyk in WT iMG (*n* = 3 independent experiments; Tukey's multiple comparisons test, mean ± s.e.m.). **d**, Schematic illustrating ATV and TREM2 Fab valency effects on pSyk signaling. Antibodies include anti-TREM2 and ATV:TREM2 with MV and BV Fabs. **e**, hTREM2-DAP12 HEK293 cells treated with a dose response of antibodies for 5 minutes, followed by pSyk detection (*n* = 3 independent experiments; mean ± s.e.m.). **f**, pSyk is blocked by co-treatment of ATV:TREM2 and anti-TfR. hTREM2-DAP12 HEK293 cells were dosed with 100 nM TREM2 antibodies and a titration anti-TfR. pSyk was detetced 5 minutes after treatment (*n* = 3 independent experiments; mean ± s.e.m.). **g**, TfR and TREM2 co-IP. hTREM2-DAP12 HEK293 cells were treated with 100 nM per antibody for 5 minutes, followed by IP on cell lysates with anti-TREM2. TfR was detected by western blot. **h**, Co-IP quantification of western blot data in **g** (*n* = 6 independent experiments; Wilcoxon test for ISO versus anti-TREM2, two-tailed paired *t*-test for ATV:ISO versus ATV:TREM2, mean ± s.e.m.). **i**, Schematic of BioID TREM2 receptor clustering assay strategy. **j**, Representative western blot detection of biotinylated TREM2 after streptavidin IP. TREM2-BioID expression was induced 24 hours before the assay with 2 ng ml^{-1} of Dox. Cells were treated with 100 nM antibody and 2 μM biotin. **k**, Quantification of western blot from **j** (*n* = 4 independent experiments; ratio of two-tailed paired *t*-test, mean ± s.e.m.). **l**, Representative immunofluorescence images of hTREM2-DAP12 HEK293 cells stained for IgG (green), pSyk (yellow) and EEA1 (red). Cells were treated with 10 nM per antibody for 10 min. **m**, Quantification of spot intensity for IgG and pSyk immunofluorescence per cell (*n* = 3 independent experiments with 3,000–5,000 cells per condition; Tukey's multiple comparisons test, mean ± s.e.m.). **n**, Quantification of percent of IgG or pSyk spots localized within EEA1^{+} endosomes (*n* = 3 independent experiments with 3,000–5,000 cells per condition; Tukey's multiple comparisons test, mean ± s.e.m.).

We then performed gene set enrichment analysis (GSEA) (Fig. 1h and Supplementary Table 5). Cluster 3 showed modest enrichment of glycolysis, oxidative phosphorylation and lipid metabolism signatures, suggesting that amyloid pathology imposes a metabolic demand on microglia. Metabolic signatures were further upregulated by ATV:4D9 in clusters 2 and 4. ATV:4D9 reduced amyloid-induced cluster 3 and

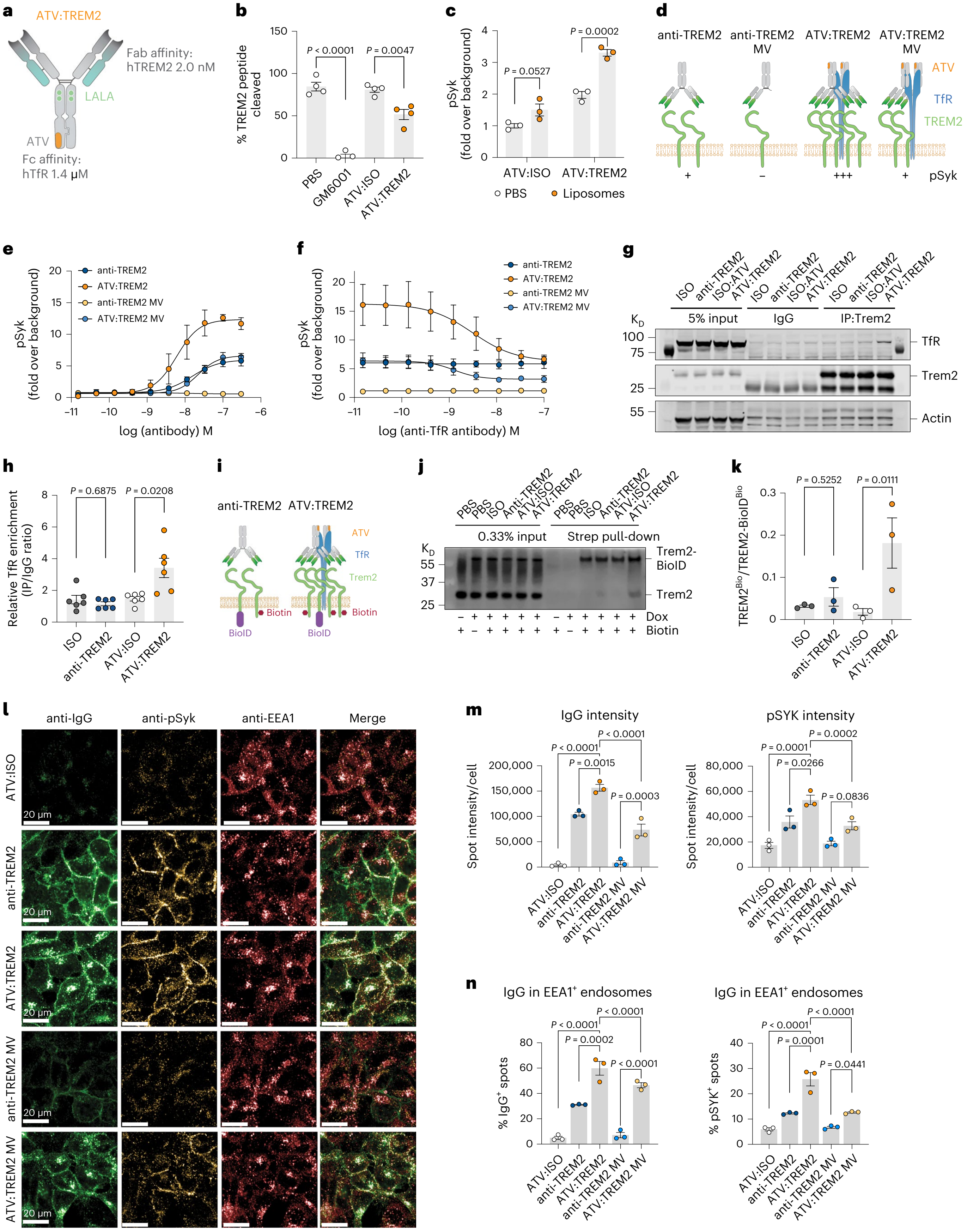

Table 1 | Comparative TREM2 antibody binding affinity and cellular activity

Assay	Analyte	Anti-TREM2	ATV:TREM2	ATV:4D9
SPR binding K_D (M)	hTREM2	2.46×10^{-9}	2.00×10^{-9}	No binding
SPR binding K_D (M)	msTREM2	No binding	No binding	3.16×10^{-10}
SPR binding K_D (M)	hTfR	No binding	1.43×10^{-6}	9.09×10^{-7}
Macrophage survival EC_{50} (M)		2.7×10^{-9}	4.1×10^{-9}	4.1×10^{-9}

SPR binding and macrophage survival potency values for ATV:4D9, anti-TREM2 and ATV:TREM2. Macrophage survival was determined using plate-coated antibody with ATP quantification for cell viability. ATV:4D9-induced survival was tested on bone marrow-derived macrophages (BMDMs) from WT;TfR$^{mu/hu}$ mice.

expanded metabolic clusters 2 and 4 in *App*^{SAA};TfR$^{mu/hu}$ mice (Fig. 1d,c). Therefore, ATV:4D9 promoted transcription of multiple metabolic pathways in microglia. We conducted IHC on brain sections and detected increased CD74 and AXL in a subset of IBA1$^+$ microglia, consistent with the transcriptional profiling (Extended Data Figs. 1d and 2f–l).

We next observed profound morphological changes consistent with a responsive microglial state, including higher fractal dimension, convexity, solidity and a larger number of short branches 1 day and 7 days after ATV:4D9 dose. These responsive morphological features were reversible, as homeostatic features were observed 14 days and 28 days after dosing (Extended Data Fig. 2a,c). Thus, ATV:4D9 induced dynamic microglial states transcriptionally and morphologically.

ATV:TREM2 is a human TREM2 stalk region binding antibody

Next, we sought to generate an antibody with similar properties to ATV:4D9 targeting human TREM2 for the clinic (Extended Data Fig. 3a). Rodents were immunized with the human TREM2 extracellular domain (amino acids 19–172) to enable discovery of a novel human TREM2-activating antibody. This antibody was engineered with an effectorless Fc[41] (Supplementary Table 1) and ATV[35] (Fig. 2). Binding affinity of ATV:TREM2 to human TREM2 was 2 nM, whereas binding to human TfR was 1.4 µM, by surface plasmon resonance (SPR) (Fig. 2a and Table 1). ATV:TREM2 binds the TREM2 stalk region, N-terminal to the ADAM17 cleavage site (residues 143–149, FPGESES) determined by hydrogen–deuterium exchange (Extended Data Fig. 3b). ATV:TREM2 has an apparent 4 nM cell binding potency (Extended Data Fig. 3c) and binds endogenous TREM2 on human induced pluripotent stem cell (iPSC)-derived WT microglia (iMG) by fluorescence-activated cell sorting (FACS), whereas *TREM2* knockout (KO) iMG showed no detectable difference compared to isotype control (Extended Data Fig. 3d). Therefore, the human-specific ATV:TREM2 demonstrated similar properties to ATV:4D9 based on high-affinity binding of a stalk region epitope, TREM2 signaling activation, and functional effects in relevant myeloid cells[31] (Extended Data Fig. 3 and Table 1).

ATV:TREM2 reduces shedding and activates TREM2 signaling

To elucidate ATV:TREM2 mechanisms of action, we examined shedding blocking as observed with 4D9 (ref. 31). ATV:TREM2 partially blocked stalk peptide cleavage by ADAM17, whereas the control inhibitor GM6001 completely blocked shedding (Fig. 2b). This biochemical activity is consistent with the ability of ATV:TREM2 to reduce soluble TREM2 in a cell-based assay (Extended Data Fig. 3e) and in the CSF of WT;TfR$^{mu/hu}$ mice treated with ATV:4D9 (Supplementary Fig. 1l).

TREM2 signals upon binding phosphatidylserine (PS) and other anionic lipids[3,10]. Therefore, we determined if antibody binding affects lipid signaling. iMG co-treated with PS liposomes and ATV:TREM2 showed enhanced signaling (Fig. 2c and Extended Data Fig. 3f). To determine if ATV:TREM2 engages a functional cellular response, we examined rescue of survival defects in primary human macrophages cultured in low macrophage colony-stimulating factor (M-CSF) and found a potent survival rescue with a half-maximal effective concentration (EC_{50}) of ~1 nM (Extended Data Fig. 3g). Together, these data show that ATV:TREM2 does not block lipid ligands and signals sufficiently to promote cellular function.

TREM2 receptor clustering is enhanced by ATV TfR binding

Previous studies demonstrated that TREM2-activating antibodies require bivalent binding[31,33]. To test valency properties of ATV:TREM2, we compared bivalent (BV) and monovalent (MV) versions for the impact on pSyk signaling. Whereas anti-TREM2 MV showed no activity (Fig. 2d,e), ATV:TREM2 MV displayed similar activity as anti-TREM2 BV, and ATV:TREM2 BV increased maximal signaling and potency (Fig. 2d,e). Thus, ATV enhances TREM2 Fab activity. These effects required ATV-TfR binding as a competitive TfR antibody inhibited ATV:TREM2's pSyk potentiation (Fig. 2f).

To investigate receptor interactions, we performed co-immunoprecipitation (co-IP) with a TREM2 antibody and probed for TfR by western blot (Fig. 2g). We found a ~2-fold increase in TfR in the IP fraction isolated from ATV:TREM2 but not anti-TREM2-treated hTREM2-DAP12 HEK293 cells (Fig. 2g,h). A TfR–TREM2 complex was observed in the reciprocal co-IP (Extended Data Fig. 4a,b). Therefore, ATV:TREM2 mediates direct TREM2–TfR interactions. To test TREM2 receptor clustering, we used biotin proximity labeling (Fig. 2i), in which a doxycycline (Dox)-inducible TREM2 fusion protein was tagged intracellularly with BioID2, a mini biotin ligase[42], and transfected this construct in hTREM2-DAP12 HEK293 cells to generate cells expressing both untagged and BioID-tagged TREM2. ATV:TREM2 drove significant TREM2 biotinylation detected by western blot, compared to anti-TREM2 or isotype (Fig. 2j,k). This provides biochemical evidence that ATV:TREM2 mediates receptor clustering (Fig. 2d,i).

ATV:TREM2 promotes pSyk via TREM2 and TfR binding in *cis*

Next, we sought to elucidate whether ATV:TREM2 enhances pSyk in *cis* or *trans*. In *cis*, TfR and TREM2 are co-expressed on the same cell; in *trans*, receptor expression is on adjacent cells (Extended Data Fig. 4c). To distinguish between these possibilities, pSyk was detected upon antibody pre-treatment in a mix of TfR^{WT} and TfR^{RNAi} hTREM2-DAP12 HEK293 cells, in which the latter cells' TfR is knocked down with RNAi (Extended Data Fig. 4d). Antibody-treated cells were plated either separately or pre-mixed and then plated. pSyk activity was similar in both conditions, supporting a *cis* mechanism (Extended Data Fig. 4e). Exogenous addition of ATV:TREM2–TfR immuno-complexes with TfR knockdown did not enhance pSyk activity (Extended Data Fig. 4f), in contrast to artificial clustering by a secondary anti-Fc antibody that elevated pSyk (Extended Data Fig. 4g). Taken together, these studies indicate that ATV:TREM2 mediates TfR–TREM2 binding in *cis* to enhance TREM2 signaling.

ATV-driven internalization results in endosomal signaling

Because TfR undergoes constitutive internalization and endosomal recycling, we hypothesized that ATV could impact intracellular trafficking or subcellular localization of TREM2. We tracked TREM2 by immunofluorescence in ATV-treated hTREM2-DAP12 HEK293 cells and observed rapid surface downregulation (Extended Data Fig. 4h). Total cellular levels remained constant, suggesting that TREM2 is internalized but not degraded (Extended Data Fig. 4h). ATV:TREM2 was detected intracellularly, whereas anti-TREM2 showed surface localization (Fig. 2l). ATV:TREM2 signal intensity was higher than anti-TREM2 (Fig. 2m). ATV:TREM2 BV and MV increased pSyk compared to anti-TREM2 (Fig. 2l,m). With equivalent cellular IgG levels, ATV:TREM2 elicited slightly higher pSyk compared to anti-TREM2 (Extended Data Fig. 4l). These data suggest that ATV:TREM2 enhances TREM2 signaling not solely by increasing bound antibody but likely due to TfR-mediated intracellular trafficking.

To examine this hypothesis, we quantified antibody (IgG) and pSyk co-localization to EEA1$^+$ endosomes and TfR$^+$ recycling endosomes

(Extended Data Fig. 4j). ATV:TREM2 and pSyk were detected in EEA1$^+$ and TfR$^+$ endosomes approximately two-fold higher than anti-TREM2 (Fig. 2l,n and Extended Data Fig. 4k,l). Therefore, ATV:TREM2 becomes localized to endosomes with pSyk. These studies demonstrate dual mechanisms of action in which ATV enhances TREM2 antibody function via TfR–TREM2 clustering and endosomal signaling. These studies elucidate mechanisms of action for ATV:TREM2 mediated by TfR engagement.

mTOR and *PLCG2* are required for microglial proliferation

Next, we sought to identify signaling pathways by which ATV:TREM2 instructs microglial physiological responses. In human iMG[25,43], ATV:TREM2 induced phosphorylation of key modulators of the mTOR pathway, including mTOR, AKT, RPS6 and GSK3b, whereas changes in p4EBP1 or pERK1/2 were not detected (Fig. 3a–e and Extended Data Fig. 5a,b). Total protein levels of mTOR and AKT were unaltered (Extended Data Fig. 5c,d). Concurrently, ATV:TREM2 increased proliferation in WT but not *TREM2* KO or *PLCG2* KO iMG (Fig. 3f–h), showing this activity is specific and requires *PLCG2* (refs. 22, 24, 25). The mTOR inhibitor AZD8055 blocked ATV:TREM2-induced mTOR signaling (Extended Data Fig. 5e,f), reduced EdU labeling, and blocked increased iMG cell numbers (Fig. 3h–j). Therefore, ATV:TREM2-driven microglial proliferation requires mTOR signaling.

Next, we found that ATV:TREM2 induced a cell cycle G2M checkpoint gene signature in WT iMG by bulk RNA-seq, distinct pathway biology compared to other stimuli, such as TGFβ, lipopolysaccharide (LPS) or IFNγ (Fig. 3k and Supplementary Table 4). ATV:TREM2-treated WT iMG showed nominal cytokine release compared to LPS (Extended Data Fig. 5g). These data show that ATV:TREM2 promotes microglia proliferation via mTOR and PLCG2 and is biologically distinct from other innate immune stimuli.

ATV:TREM2 improved pharmacodynamic responses in vivo

To explore if our in vitro iMG findings translated in vivo, we generated a *TREM2* BAC transgenic (tg) mouse model expressing human TREM2 (Supplementary Fig. 3a–c). This model was bred to WT;TfR$^{mu/hu}$ mice for pharmacokinetic and pharmacodynamic studies. Brain concentrations of ATV:TREM2 increased dose dependently and were higher than anti-TREM2 (Fig. 4a and Extended Data Fig. 6a), demonstrating that ATV:TREM2 has improved brain exposure after a single IV dose. Using IBA1 immunostainings coupled with EdU labeling to detect proliferating microglia, we found that ATV:TREM2 induces a dose-dependent increase in IBA1$^+$ and IBA1$^+$ EdU$^+$ microglia, whereas anti-TREM2 showed no effect (Fig. 4b,c). These results indicate that ATV:TREM2 enhances microglia proliferation in vivo compared to anti-TREM2 at similar brain exposures.

CSF1R is expressed on microglia and is essential for survival[44]. A TREM2 antibody elevated soluble CSF1R (sCSF1R) in CSF of healthy volunteers[32]; therefore, it represents a potential pharmacodynamic biomarker. ATV:TREM2, but not anti-TREM2, increased brain and CSF CSF1R levels in a dose-dependent manner, with maximal response at 10 mg kg^{-1} (Fig. 4d,e). As TREM2 can affect microglia in a sex-dependent manner[45], we confirmed that ATV:TREM2 increased CSF1R in males and females (Extended Data Fig. 6b,c and Supplementary Table 3), showing no significant sex differences.

To elucidate effects of ATV affinity, two additional variants were engineered: one with higher TfR affinity (110 nM) and one with lower affinity (8,000 nM), compared to the 1,100 nM TfR affinity used in all other studies. WT;human TREM2 tg;TfR$^{mu/hu}$ mice were treated with variable doses to achieve similar brain exposure (Extended Data Fig. 6d). ATV^{8000nM}:TREM2 reached similar brain concentrations as ATV^{1100nM}:TREM2 but did not induce CSF1R (Extended Data Fig. 6e,f), whereas ATV^{110nM}:TREM2 induced similar CSF1R levels as ATV^{1100nM}:TREM2, suggesting that ATV requires an affinity threshold to enhance TREM2 Fab activity.

ATV:TREM2 enhances microglial phagocytosis ex vivo

Previous studies demonstrated that TREM2 antibodies enhance microglial phagocytosis in vitro[31,34]. To determine the impact of ATV:TREM2 on this function, we administered antibodies in vivo and then evaluated microglial uptake of myelin or Aβ ex vivo. WT;human TREM2 tg;TfR$^{mu/hu}$ mice were IV dosed with isotype control, ATV:TREM2 or anti-TREM2; brain microglia were harvested 2 days later, incubated with fluorescently labeled substrates (Extended Data Fig. 6g); and phagocytosis was quantified by FACS (Extended Data Fig. 6h). ATV:TREM2 increased phagocytosis of pHrodo-green$^+$ myelin and FAM-labeled Aβ compared to isotype control (Fig. 4f,g). In contrast, anti-TREM2 at similar brain concentrations (Extended Data Fig. 6l) did not alter microglial myelin uptake (Fig. 4f). Moreover, ATV:TREM2 upregulated genes associated with phagocytosis, such as *Axl*, *Itgax* and *Lgals3* (Extended Data Fig. 6j).

ATV:TREM2 demonstrates enhanced brain uptake and catabolism

We next determined the kinetics of uptake and catabolism of ATV:TREM2 using longitudinal single-photon emission computed tomography (SPECT) imaging with radiolabeled antibodies. Radiometabolites generated from [^{125}I]SIB-labeled antibodies are rapidly effluxed, whereas those from [^{111}In]DOTA labeling have residualizing properties with cumulative uptake due to cellular retention[46]. [^{125}I]SIB-labeled ATV:TREM2 and ATV:ISO showed substantial clearance from brain (Extended Data Fig. 7a,b). In contrast, [^{111}In]DOTA-labeled ATV:TREM2 showed a persistent elevated signal over the 96-hour time course (Extended Data Fig. 7a,c).

ATV:TREM2 showed a high catabolic rate in all brain regions examined (Extended Data Fig. 7d), providing a mechanistic explanation for lower brain concentrations of ATV:TREM2 compared to ATV:ISO control observed in multiple studies (Fig. 1k and Extended

Fig. 3 | Microglial proliferation induced by ATV:TREM2 requires mTOR signaling and PLCG2. a, Representative western blot images for p-mTOR (S2448), pAKT (S473), pGSK3b (S9) and pRPS6 (S235/236) in WT iMG treated with 100 nM ATV:TREM2 or isotype control. **b**–**e**, Quantification of mTOR-S2448 (**b**), AKT-S473 (**c**), RPS6-S235/236 (**d**) and GSK3b-S9 (**e**) phosphorylation levels were normalized to actin. Relative expression was calculated by normalizing to vehicle control (PBS) for each experiment ($n = 10$ independent experiments (**b**–**d**) and $n = 9$ independent experiments (**e**); two-tailed paired *t*-test, mean ± s.e.m.). **f**, ATV:TREM2 induces proliferation in WT iMG but not TREM2 KO iMG. WT or TREM2 KO iMG were treated with 100 nM ATV:TREM2 or isotype control for 96 hours. Forty-eight hours after dose, 20 µM EdU was added to media. The proliferation index was calculated as percentage of EdU$^+$ cells normalized to vehicle control (PBS) ($n = 3$ independent experiments; two-tailed multiple-paired *t*-test, mean ± s.e.m.). **g**, Quantification of WT and *PLCG2* KO iMG proliferation. iMG were treated with 100 nM ATV:TREM2 or ATV:ISO ($n = 4$ independent experiments (WT) and $n = 3$ independent experiments (*TREM2* KO); two-tailed multiple-paired *t*-test, mean ± s.e.m.). **h**, Representative images of WT iMG proliferation. Cells were treated with vehicle (DMSO) or mTOR inhibitor AZD8055 (AZD). EdU$^+$ iMG are marked with open arrow. **i**, Quantification of WT iMG proliferation treated with mTOR inhibitor AZD8055. 20 nM AZD8055 was co-dosed with 100 nM ATV:TREM2 for 96 hours ($n = 5$ independent experiments (DMSO) and $n = 4$ independent experiments (AZD); two-tailed multiple-paired *t*-test, mean ± s.e.m.). **j**, Nuclei quantification of iMG co-treated with ATV:TREM2 and AZD. Relative nuclei count was normalized to vehicle control (PBS) for each experiment ($n = 5$ independent experiments (DMSO) and $n = 4$ independent experiments (AZD); two-tailed unpaired *t*-test, mean ± s.e.m.). **k**, RNA-seq of iMG treated for 4 days with PBS, 100 nM ATV:ISO or ATV:TREM2 or 10 ng ml^{-1} LPS, 20 ng ml^{-1} TGFβ or 20 ng ml^{-1} IFNγ. Relative expression (z-scores) of the topmost upregulated or downregulated genes selected from pathways of interest. Pathway definitions were taken from the hallmark MSigDB collection; genes shown are a subset of those found in the leading edge of the gene set for each category.

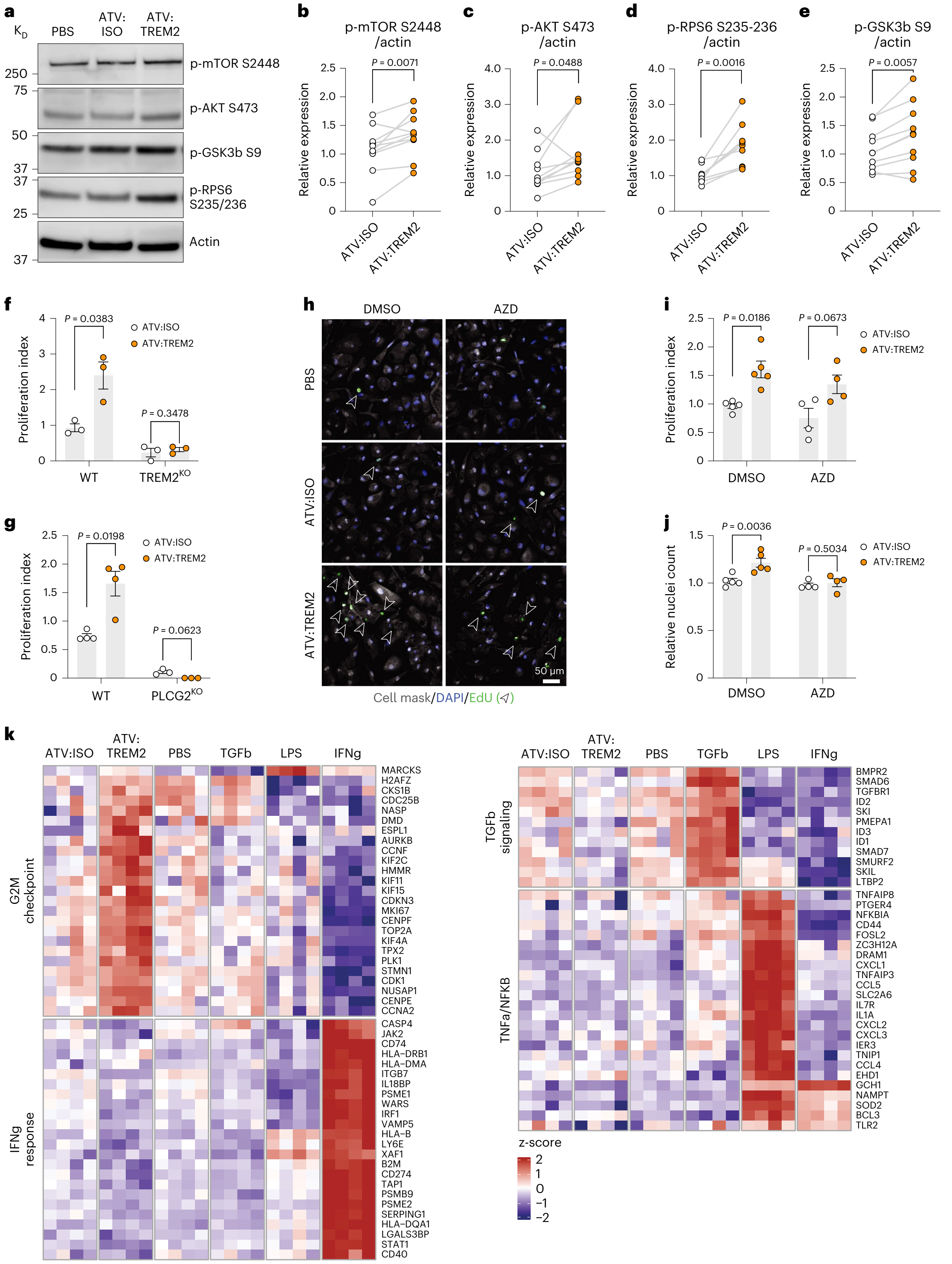
a
K_D
PBS
ATV: ISO
ATV: TREM2
250
75
50
37
37
25
37
p-mTOR S2448
p-AKT S473
p-GSK3b S9
p-RPS6 S235/236
Actin
b
p-mTOR S2448 /actin
P = 0.0071
c
p-AKT S473 /actin
P = 0.0488
d
p-RPS6 S235-236 /actin
P = 0.0016
e
p-GSK3b S9 /actin
P = 0.0057
Relative expression
ATV:ISO
ATV:TREM2
f
Proliferation index
P = 0.0383
P = 0.3478
○ ATV:ISO
● ATV:TREM2
WT
$TREM2^{KO}$
g
Proliferation index
P = 0.0198
P = 0.0623
○ ATV:ISO
● ATV:TREM2
WT
$PLCG2^{KO}$
h
DMSO
AZD
PBS
ATV:ISO
ATV:TREM2
50 μm
Cell mask/DAPI/EdU (◁)
i
Proliferation index
P = 0.0186
P = 0.0673
○ ATV:ISO
● ATV:TREM2
DMSO
AZD
j
Relative nuclei count
P = 0.0036
P = 0.5034
○ ATV:ISO
● ATV:TREM2
DMSO
AZD
k
ATV:ISO
ATV: TREM2
PBS
TGFb
LPS
IFNg
G2M checkpoint
MARCKS
H2AFZ
CKS1B
CDC25B
NASP
DMD
ESPL1
AURKB
CCNF
KIF2C
HMMR
KIF11
KIF15
CDKN3
MKI67
CENPF
TOP2A
KIF4A
TPX2
PLK1
STMN1
CDK1
NUSAP1
CENPE
CCNA2
IFNg response
CASP4
JAK2
CD74
HLA-DRB1
HLA-DMA
ITGB7
IL18BP
PSME1
WARS
IRF1
VAMP5
HLA-B
LY6E
XAF1
B2M
CD274
TAP1
PSMB9
PSME2
SERPING1
HLA-DQA1
LGALS3BP
STAT1
CD40
TGFb signaling
BMPR2
SMAD6
TGFBR1
ID2
SKI
PMEPA1
ID3
ID1
SMAD7
SMURF2
SKIL
LTBP2
TNFa/NFKB
TNFAIP8
PTGER4
NFKBIA
CD44
FOSL2
ZC3H12A
DRAM1
CXCL1
TNFAIP3
CCL5
SLC2A6
IL7R
IL1A
CXCL2
CXCL3
IER3
TNIP1
CCL4
EHD1
GCH1
NAMPT
SOD2
BCL3
TLR2
z-score
2
1
0
−1
−2

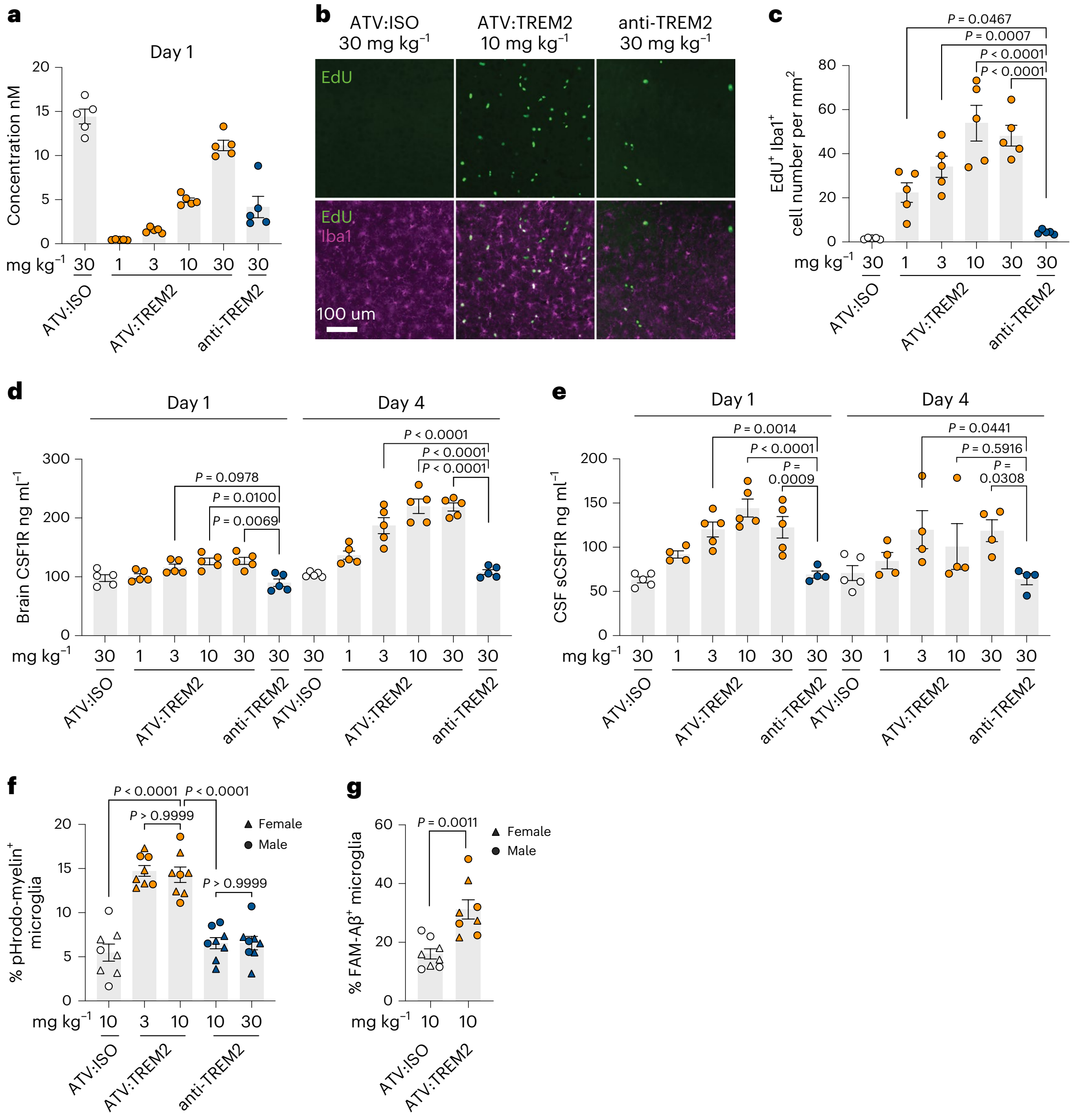

Fig. 4 | ATV:TREM2 demonstrates improved brain exposure and pharmacodynamic microglial responses compared to anti-TREM2. **a**–**e**, Four-day single-dose study. **a**, ELISA detection of antibodies in whole brain lysates for mice dosed with ATV:TREM2 (1, 3, 10 or 30 mg kg^{-1}) and anti-TREM2 (30 mg kg^{-1}) 1 day after dose (n = 5 mice per group). **b**, Microglia detected by IBA1 staining (purple), and proliferative cells were detected by EdU labeling (green) 4 days after dose. **c**, Quantification of IBA1/EdU staining (n = 5 mice per group; Dunnett's multiple comparisons test, mean ± s.e.m.). **d**, CSF1R detected by ELISA in whole brain lysate (n = 5 mice per group; Kruskal–Wallis test for day 1 and Dunnett's multiple comparisons test for day 4). **e**, CSF1R detected by ELISA in CSF (n = 5 mice per group for day 1 (30 mg kg^{-1} ATV:ISO); day 1 (3 mg kg^{-1} ATV:TREM2); day 1 (10 mg kg^{-1} ATV:TREM2); day 1 (30 mg kg^{-1} ATV:TREM2); day 4 (30 mg kg^{-1} ATV:ISO). n = 4 mice per group for rest and Dunnett's multiple comparisons test for day 1; Kruskal–Wallis test for day 4, mean ± s.e.m.). **f**,**g**, Ex vivo microglial phagocytosis for different substrates. Myelin debris (**f**) (n = 8 mice per group; Dunnett's multiple comparisons test) and Aβ (**g**) (n = 8 mice per group; two-tailed unpaired t-test, mean ± s.e.m.). **a**–**g**, Circle represents male mice, and triangle represents female mice.

Data Fig. 6a,l). Notably, SPECT imaging showed that ATV:TREM2 significantly improved brain biodistribution compared to anti-TREM2. Taken together, these results demonstrate that ATV:TREM2 is broadly distributed throughout the brain, and acute TREM2 activation is sufficient to mediate sustained microglial responses, as effects persist after antibody clearance.

We assessed peripheral biodistribution and systemic safety in WT;TfR$^{mu/hu}$ mice because TfR is broadly expressed, and TREM2 is present on myeloid cells. We observed higher concentrations of ATV:ISO and ATV:4D9 relative to 4D9 in tissues with high TfR, such as brain and bone marrow (Supplementary Fig. 2a,b). Similar biodistribution was observed across all three treatment groups in spleen, plasma and lung (Supplementary Fig. 2c–e). Overall, these data suggest that ATV:4D9 biodistribution is largely driven by TfR rather than TREM2 binding. No histopathological findings, including no changes to immune cells, were observed in the bone, bone marrow, brain, heart, kidney, liver, lung, lymph node, spleen, intestine, thymus and sciatic nerve when compared to vehicle control in a 12-week study of ATV:4D9 in WT;TfR$^{mu/hu}$ mice dosed weekly at 10 mg kg^{-1}.

ATV:TREM2 enhances mitochondrial metabolism in microglia

We then sought to elucidate the ability of ATV:TREM2 to modulate disease-relevant microglial functions. Previous studies demonstrated that *TREM2* KO microglia are defective in clearing lipid-rich myelin debris[10,25,47]; therefore, we quantified lipid droplets by BODIPY staining in WT iMG treated with purified myelin followed by ATV:TREM2 and found reduced BODIPY staining compared to an isotype control (Fig. 5a). We next used liquid chromatography–mass spectrometry (LC–MS) to resolve lipid species and observed significant reductions in several triglycerides (TGs) (Fig. 5b,c and Extended Data Fig. 8a), a known component of lipid droplets[48,49]. Additionally, numerous acyl carnitine species were increased (Fig. 5b,c and Extended Data Fig. 8a). ATV:TREM2-mediated lipid catabolism required PLCγ2, as no effects on TGs were observed in *PLCG2* KO iMG (Fig. 5d and Extended Data Fig. 8b), further indicating that PLCγ2 acts downstream of TREM2 for lipid metabolism[25].

Because ATV:TREM2 concomitantly reduced TGs and increased acyl carnitines, a byproduct of mitochondrial fatty acid metabolism[50], ATV:TREM2 may promote mitochondrial function. Notably, both *TREM2* KO and *PLCG2* KO iMG showed impaired mitochondrial respiration under substrate-limiting conditions to isolate fatty acid metabolism (Fig. 5e and Extended Data Fig. 8c). Conversely, ATV:TREM2 increased maximal respiration and spare capacity (Fig. 5f and Extended Data Fig. 8d), demonstrating that ATV:TREM2 imparts metabolic flexibility and increased energetic capability in iMG. TREM2 and PLCγ2 were required for this activity (Extended Data Fig. 8e,f). The carnitine palmitoyltransferase 1 (CPT-1) inhibitor etomoxir blocked ATV:TREM2-driven increased respiration (Fig. 5f), suggesting that CPT-1, an enzyme that mediates acylation of free fatty acids and translocation into the mitochondria, is also required. ATV:TREM2 thus improves mitochondrial metabolism via fatty acid oxidation, consistent with its ability to clear TGs stored in lipid droplets. ATV:TREM2 also strongly increased mitochondrial oxidation of glucose, which was blocked by the mitochondrial pyruvate carrier (MPC) inhibitor UK5099 (Fig. 5g,h). Together, these results indicate that ATV:TREM2 increases the energetic capacity of microglia by promoting fatty acid oxidation and aerobic respiration via glucose catabolism.

To further investigate the effects of ATV:TREM2 on mitochondria, we assessed membrane potential with tetramethylrhodamine ethyl ester (TMRE) staining and found that ATV:TREM2 increased TMRE intensity by high-content imaging in iMG (Fig. 5i,j). To determine whether mitochondrial structure is impacted by ATV:TREM2, we performed super-resolution microscopy, which revealed increased networked mitochondria morphology (Fig. 5j,k). Importantly, networked mitochondria have been shown to correlate with increased oxidative phosphorylation and catabolism[51,52], consistent with ATV:TREM2's ability to boost microglial respiration.

We next examined whether this metabolic activity could be detected in vivo, so we performed RNA-seq on microglia isolated from WT;hTREM2 tg;TfR$^{mu/hu}$ mice dosed with 10 mg kg^{-1} of ATV:TREM2, ATV:ISO or vehicle control. ATV:TREM2 upregulated a significant transcriptional response at 1 day compared to isotype or vehicle, which was attenuated by day 4 (Fig. 5l). Strikingly, ATV:TREM2 increased oxidative phosphorylation and glycolysis pathway genes (Fig. 5m), consistent with increased metabolic functions in iMG. The top pathways regulated by ATV:TREM2 are shown in Extended Data Fig. 8g, and a complete gene list is provided in Supplementary Table 4.

ATV:TREM2 increases brain microglia activity in an AD model

To investigate the effects of ATV:TREM2 using brain imaging, we crossed the hTREM2 tg;TfR$^{mu/hu}$ mice to the 5×FAD model[53] and monitored brain microglial activity by [^{18}F]GE-180 18-kDa translocator protein positron emission tomography (TSPO-PET). Increased mitochondrial TSPO expression is associated with responsive microglia[54], and TREM2 LOF brains exhibit lower TSPO-PET signal compared to WT controls[55,56]. Therefore, TSPO-PET imaging could be an indicator of ATV:TREM2 function in vivo.

TSPO-PET was assessed in 5×FAD;hTREM2 tg;TfR$^{mu/hu}$ and WT;hTREM2 tg;TfR$^{mu/hu}$ mice dosed with ATV:TREM2 and an isotype control at 1, 4, and 8 days after dose. ATV:TREM2 increased cortical TSPO-PET signal in 5×FAD;hTREM2 tg;TfR$^{mu/hu}$ with significant differences at day 8 compared to an isotype control (Fig. 6a,b). TSPO signal in WT;hTREM2 tg;TfR$^{mu/hu}$ mice was detected at a lower baseline compared to 5×FAD. In WT mice, ATV:TREM2 treatment resulted in a small but statistically significant increase in TSPO signal intensity at day 8 compared to the isotype control (Fig. 6a,c). Therefore, ATV:TREM2 increased mitochondrial TSPO, indicating elevated microglial activity in vivo.

ATV:TREM2 increases brain glucose metabolism in an AD model

Brain glucose hypometabolism is an early feature of AD[57] and is associated with more rapid cognitive decline[58]. Microglial activation state can contribute to glucose metabolism in the brain detected by FDG-PET imaging[54]. Additionally, TREM2 LOF reduced brain glucose metabolism in aged and amyloid mouse models[54–56], implicating TREM2 in regulating brain metabolic activity. Therefore, we hypothesized that ATV:TREM2 could impact brain glucose metabolism. Cortical FDG-PET imaging showed that ATV:TREM2 treatment increased FDG-PET signal compared to isotype control in 5×FAD;hTREM2 tg;TfR$^{mu/hu}$ mice (day 1: +15%, day 4: +19%, day 8: +27%), whereas no effect was observed in WT;hTREM2 tg;TfR$^{mu/hu}$ mice (day 1: −5%, day 4: −3%, day 8: −3%) (Fig. 6d,f). Notably, TfR protein levels were similar in WT and AD mouse models (Supplementary Fig. 4a), suggesting that differences in TfR expression do not contribute PET imaging findings. Human TREM2 levels were elevated in sorted microglia from 5×FAD mice compared to WT, as expected[11,59] (Supplementary Fig. 4b).

Fig. 5 | ATV:TREM2 drives metabolism through mitochondrial fatty acid oxidation and *PLCG2*-dependent respiration in microglia. a, Representative microscopy images from iMG treated with 10 µM oleic acid and then 100 nM ATV:ISO or ATV:TREM2 for 48 hours. BODIPY fluorescence (shown in green) was quantified ($n = 5$ independent experiments; two-tailed paired t-test, mean ± s.e.m.). **b**, Heat map of LC–MS analysis for TG species and acyl carnitines modulated by ATV:TREM2 in iMG treated with myelin. Plotted values are log$_2$-transformed raw counts and scaled by row. **c**,**d**, ATV:TREM2 reduces TGs and increases acyl carnitines in WT iMG treated with myelin (**c**) ($n = 6$ independent experiments (TG) and $n = 3$ independent experiments (acyl carnitines); two-tailed paired t-test, mean ± s.e.m.) but not *PLCG2* KO iMG treated with myelin (**d**) ($n = 3$ independent experiments; two-tailed paired t-test, mean ± s.e.m.). **e**, Seahorse fatty acid oxidation OCR respiration measurements in *TREM2* KO and *PLCG2* KO iMG ($n = 3$ independent experiments; mean ± s.e.m.). **f**, ATV:TREM2 increases maximal respiration in WT iMG detected with Seahorse fatty acid oxidation OCR measurements ($n = 7$ independent experiments; two-tailed paired t-test, mean ± s.e.m.). The CPT-1 inhibitor etomoxir blocks the effect of ATV:TREM2 on respiration ($n = 5$ independent experiments; two-tailed paired t-test, mean ± s.e.m.). **g**,**h**, Seahorse analysis for glucose oxidation. ATV:TREM2 was treated at 100 nM for 3 days. The ATV:TREM2 effect is blocked by an MPC inhibitor, UK5099 ($n = 4$ independent experiments; two-tailed paired t-test, mean ± s.e.m.). **i**, ATV:TREM2 increases average TMRE intensity in iMG after 3 days with 100 nM antibody ($n = 6$ independent experiments; two-tailed paired t-test, mean ± s.e.m.). **j**, Representative images of super-resolution microscopy of TMRE staining in iMG. Mitochondria were segmented into networked and punctate morphologies. **k**, Morphometric analysis of the prevalence of networked mitochondria ($n = 3$ independent experiments, two-tailed paired t-test). **l**, Volcano plots of RNA-seq analysis of microglia isolated from mice dosed with 10 mg kg^{-1} of ATV:ISO or ATV:TREM2 for 1 day, 4 days or 7 days. Red or blue indicate significantly upregulated or downregulated genes, respectively. The x axis represents log$_2$ fold change in expression compared to vehicle-treated mice, and the y axis represents $-\log_{10}$ adjusted P value. **m**, Relative expression (z-scores) of the top-most upregulated or downregulated genes at day 1 after dose selected from oxidative phosphorylation and glycolysis pathways. OCR, oxygen consumption rate.

We performed [^{18}F]florbetaben beta-amyloid-PET in 5×FAD; hTREM2 tg;TfR$^{mu/hu}$ mice to examine if regional amyloid load correlated with ATV:TREM2 effects on TSPO-PET and FDG-PET. Given the short duration of these studies, we did not anticipate changes in amyloid plaque load; however, there was significant regional association for TSPO-PET and FDG-PET at day 8 with frequency band broadening (FBB) signal, suggesting that ATV:TREM2 impacts brain regions based on amyloid load (Fig. 6g,h). These results suggest that ATV:TREM2 could rescue deficits in brain glucose metabolism, potentially ameliorating this metabolic deficit found in AD.

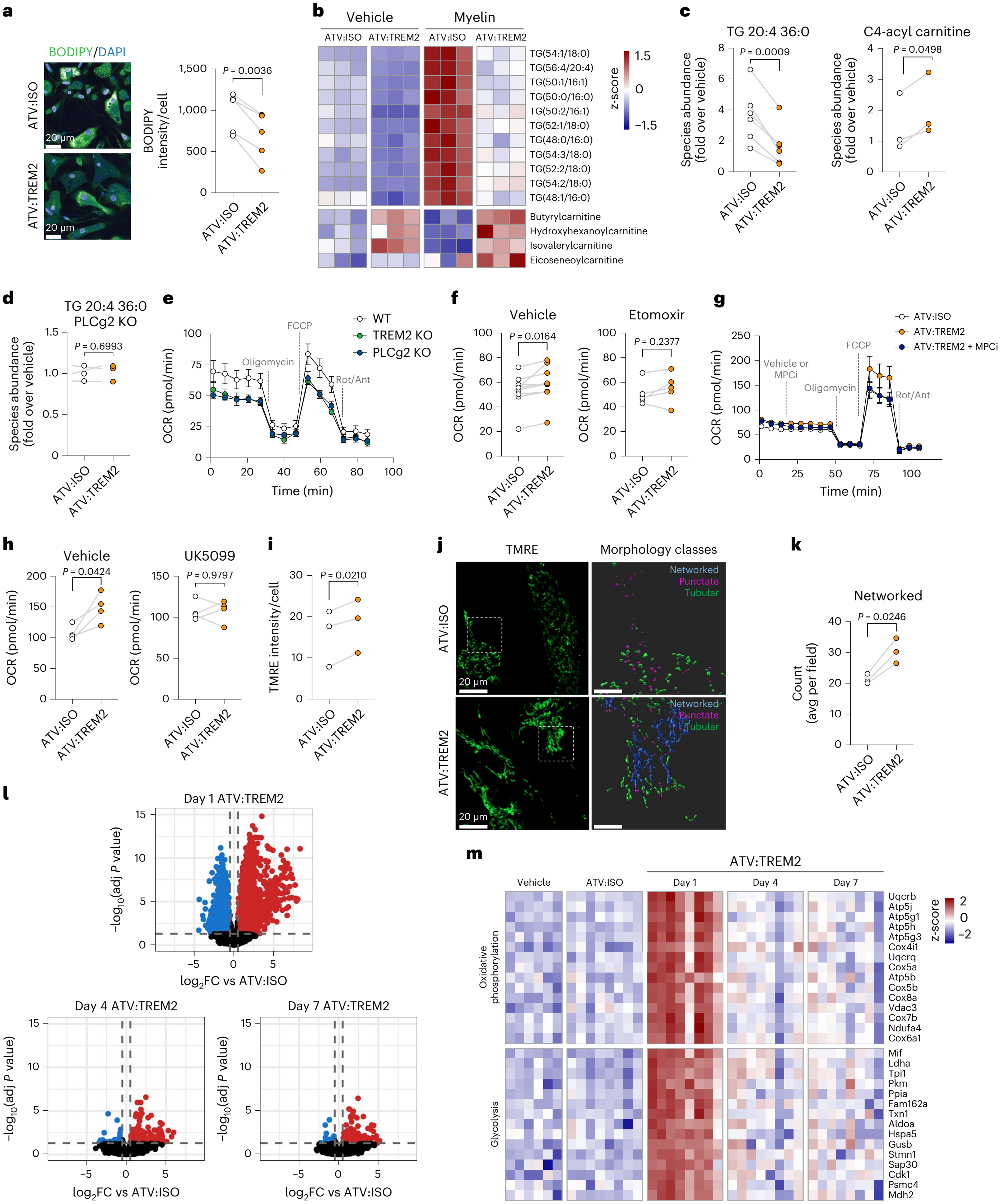

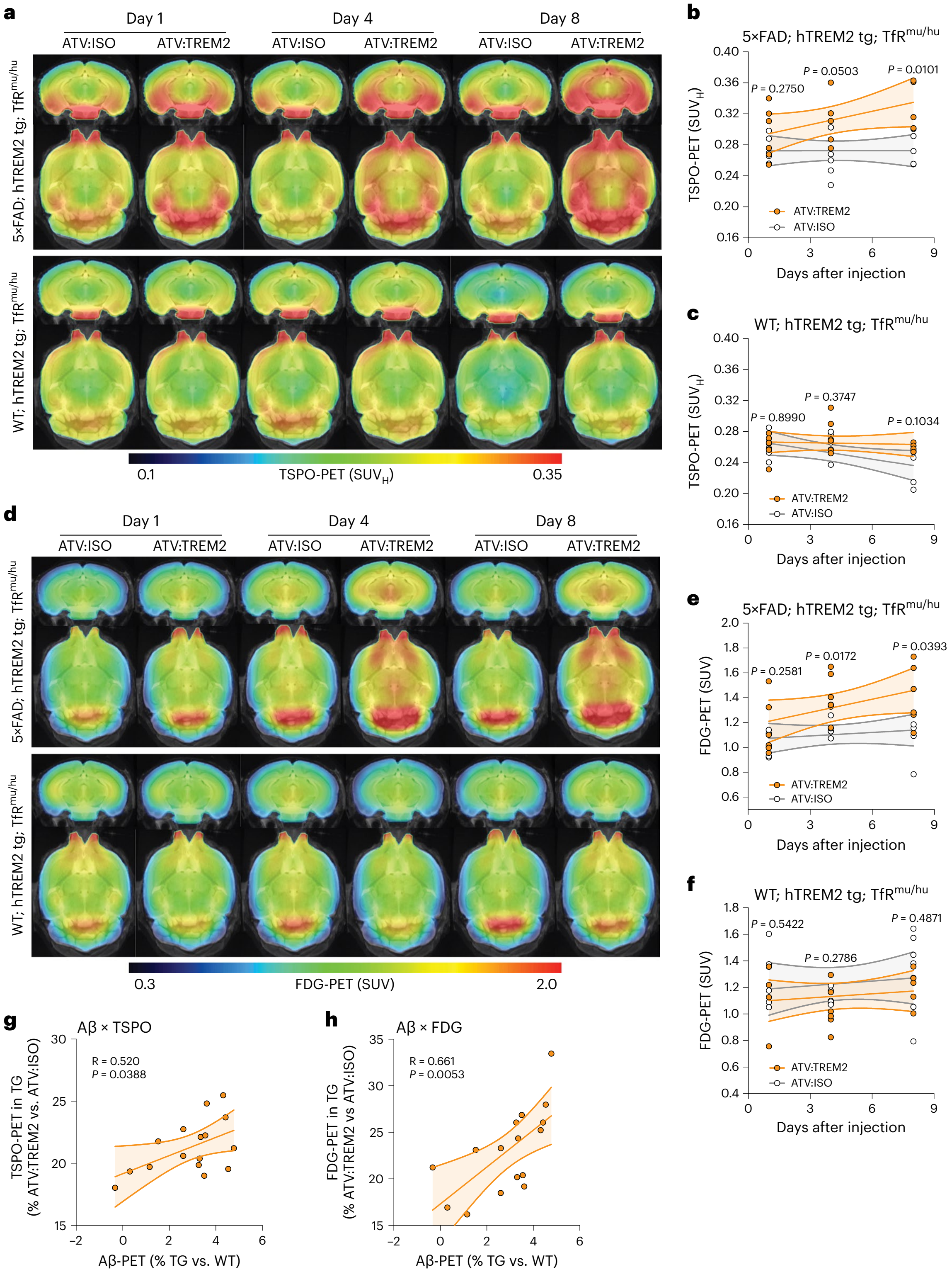

Fig. 6 | ATV:TREM2 increases brain microglial activity and glucose metabolism in an AD model. a, Coronal and axial slices show cold scaled group average images of TSPO-PET (SUV_H) projected upon a standard MRI T1-weighted atlas from 5×FAD;hTREM2 tg;$TfR^{mu/hu}$ mice (top row) or WT;hTREM2 tg;$TfR^{mu/hu}$ mice (bottom row) mice dosed with 10 mg kg^{-1} of antibody. **b**,**c**, Quantification of TSPO-PET 1, 4, and 8 days after dose in 5×FAD;hTREM2 tg;$TfR^{mu/hu}$ mice (**b**) and WT;hTREM2 tg;$TfR^{mu/hu}$ mice (**c**). Scatter plot of individual TSPO-PET (SUV_H) values. Dotted lines represent linear associations between interval after antibody dosing and TSPO-PET quantification per group and with a 95% confidence interval (*n* = 6 mice per group; two-tailed unpaired *t*-test for each timepoint, except for day 8, which used the two-tailed unpaired *t*-test with Welch's correction). **d**, Coronal and axial slices show cold scaled group average images of FDG (SUV) projected upon a standard MRI T1-weighted atlas from 5×FAD;hTREM2 tg;$TfR^{mu/hu}$ mice (top row) or WT;hTREM2 tg;$TfR^{mu/hu}$ mice (bottom row) after 10 mg kg^{-1} of antibody. **e**,**f**, Quantification of cortical glucose uptake measured by FDG-PET 1, 4, and 8 days after dose of ATV:ISO or ATV:TREM2 for 5×FAD;hTREM2 tg;$TfR^{mu/hu}$ mice (**e**) and WT;hTREM2 tg;$TfR^{mu/hu}$ mice (**f**). Scatter plot of individual FDG (SUV) values. Dotted lines represent linear associations between interval after antibody dosing and FDG-PET quantification per group with a 95% confidence interval (*n* = 6 mice per group; two-tailed unpaired *t*-test for each timepoint). **g**,**h**, Regional correlation of biomarker alterations (5×FAD;hTREM2 tg;$TfR^{mu/hu}$ versus WT;hTREM2 tg;$TfR^{mu/hu}$ mice) between FBB-PET at 5 months and TSPO-PET (SUV_H) (**g**) and FDG-PET (SUV) (**h**) at the group level.

Discussion

In this study, we describe the mechanisms of action and cellular functions of ATV-enabled anti-TREM2 biologics, including mouse-specific ATV:4D9 and human-specific ATV:TREM2. Our findings demonstrate that ATV enables improved biodistribution and activity of TREM2 antibodies. The functional genetics demonstrate that LOF TREM2 LOAD risk variants disable protective microglial responses. Therefore, promoting TREM2 to improve microglia functions is a compelling therapeutic approach. Surprisingly, ATV not only improved brain uptake and biodistribution of our TREM2 antibody; it also enhanced TREM2 signaling at the cellular level through co-engagement of TREM2 and TfR. We show that a key physiological effect of ATV:TREM2 is to improve the energetic capacity of microglia through enhanced fatty acid and glucose oxidation in mitochondria. We also demonstrate that ATV:TREM2 increased microglial activity and glucose metabolism in an amyloid mouse model via TSPO-PET and FDG-PET imaging, respectively.

The concept and generation of ATV:TREM2 was driven by the need to improve target engagement in the brain. Although the transport vehicle (TV) platform improved brain uptake for ATV:TREM2 as observed with other large molecules[35,36,60], the impact of ATV on the cellular activity of a TREM2 antibody remained an open question. We found that ATV altered TREM2 Fab function through two distinct mechanisms: (1) enhanced receptor clustering and (2) increased endosomal signaling. Because ATV:TREM2 resulted in enhanced microglia responses compared to anti-TREM2 with equivalent brain IgG concentrations, the molecular and cellular mechanisms identified in vitro are likely engaged in vivo. These observations indicate that ATV:TREM2 has superior activity in addition to enhanced brain delivery and is, therefore, a highly differentiated candidate biotherapeutic.

Previous work showed that a TREM2 antibody can activate AKT[34]; however, the cellular functions it mediates had not been demonstrated. We found that ATV:TREM2 activates mTOR signaling, which is required for microglia proliferation. Furthermore, we demonstrate that PLCγ2 is required for proliferation and metabolic pathways downstream of TREM2 in iMG. *PLCG2* KO phenocopies *TREM2* KO in iMG, showing deficient proliferation and mitochondrial respiration. These findings support a genetically validated TREM2 pathway in which PLCγ2 acts downstream and is required for diverse microglial functions induced by ATV:TREM2. Our studies provide further support for the direction of therapeutic modulation of TREM2, because an AD-protective *PLCG2* variant has been shown to be mildly hypermorphic, indicating that increased PLCγ2 activity is beneficial for disease[23,25]. Our findings indicate microglia functions with disease-modifying potential based on the link to additional AD-relevant genes.

The functional implications of human AD genetics that point to TREM2 in microglia as a modulator of disease risk remain a critical question in the field. Previous studies conducted 48 hours after TREM2 antibody dosing[32,33] show that pharmacological activation elicited transcriptional responses. However, these data had not shown specific functional effects on microglia. We show direct evidence of microglia proliferation induced by ATV:TREM2, which could help resolve pathology or serve as a renewal process to reset microglial state. The proliferative response appears limited to a subset of microglia, and factors regulating it are not yet understood. ATV:TREM2 also improved microglial phagocytosis, suggesting that ATV:TREM2 imparts multiple functions that could ameliorate disease.

A key advancement of our studies is the temporal and dose–response effects of ATV:TREM2 in vivo. Whereas previous studies evaluated TREM2 antibodies at one timepoint with a single dose[32,33], here we provide a more comprehensive view. ATV:4D9 induced durable yet reversible microglial responses by single-cell transcriptional profiling and morphometry. The ability of microglia to reverse states has recently been observed where TREM2 antagonistic antibodies reduce *Grn* LOF hyperactivation[61], indicating that microglial states are indeed tunable.

Known features of TREM2 LOF microglia include survival defects and arrest in a homeostatic low metabolic state[56,62,63] and lipid accumulation due to myelin debris[10,25]. Therefore, we sought to determine whether TREM2-related metabolic deficiencies were a secondary consequence of survival deficits or if cellular metabolism could be specifically activated by ATV:TREM2. We discovered that ATV:TREM2 promotes energetic capacity via specific metabolic pathways. Namely, ATV:TREM2 promoted mitochondrial fatty acid oxidization, in which TGs stored in lipid droplets are catabolized to increase microglial respiration. ATV:TREM2 also promoted glucose oxidation, demonstrating flexibility in substrate utilization. We hypothesized that this in vitro activity could connect to disease efficacy rationale as patients with AD and TREM2 LOF mice display hypometabolism with low FDG-PET signal[54–56,58]. ATV:TREM2 increased FDG-PET in an amyloid mouse model, thereby improving brain metabolism in a disease context. Whether ATV:TREM2 induces glucose uptake cell autonomously in microglia or influences other CNS cell types remains an open question. Taken together, our results demonstrating improved brain exposure and biodistribution of a TREM2-activating antibody capable of enhancing microglial functions and improving brain metabolism suggest that ATV:TREM2 is a differentiated therapeutic candidate for the treatment of AD.

Online content

Any methods, additional references, Nature Portfolio reporting summaries, source data, extended data, supplementary information, acknowledgements, peer review information; details of author contributions and competing interests; and statements of data and code availability are available at https://doi.org/10.1038/s41593-022-01240-0.

References

1. Wightman, D. P. et al. A genome-wide association study with 1,126,563 individuals identifies new risk loci for Alzheimer's disease. *Nat. Genet.* **53**, 1276–1282 (2021).
2. Lewcock, J. W. et al. Emerging microglia biology defines novel therapeutic approaches for Alzheimer's disease. *Neuron* **108**, 801–821 (2020).
3. Wang, Y. et al. TREM2 lipid sensing sustains the microglial response in an Alzheimer's disease model. *Cell* **160**, 1061–1071 (2015).
4. Ulland, T. K. & Colonna, M. TREM2—a key player in microglial biology and Alzheimer disease. *Nat. Rev. Neurol.* **14**, 667–675 (2018).
5. Feuerbach, D. et al. ADAM17 is the main sheddase for the generation of human triggering receptor expressed in myeloid cells (hTREM2) ectodomain and cleaves TREM2 after Histidine 157. *Neurosci. Lett.* **660**, 109–114 (2017).
6. Wunderlich, P. et al. Sequential proteolytic processing of the triggering receptor expressed on myeloid cells-2 (TREM2) protein by ectodomain shedding and γ-secretase-dependent intramembranous cleavage. *J. Biol. Chem.* **288**, 33027–33036 (2013).
7. Kleinberger, G. et al. TREM2 mutations implicated in neurodegeneration impair cell surface transport and phagocytosis. *Sci. Transl. Med.* **6**, 243ra286 (2014).
8. Takahashi, K., Rochford, C. D. & Neumann, H. Clearance of apoptotic neurons without inflammation by microglial triggering receptor expressed on myeloid cells-2. *J. Exp. Med.* **201**, 647–657 (2005).
9. Mazaheri, F. et al. TREM2 deficiency impairs chemotaxis and microglial responses to neuronal injury. *EMBO Rep.* **18**, 1186–1198 (2017).
10. Nugent, A. A. et al. TREM2 regulates microglial cholesterol metabolism upon chronic phagocytic challenge. *Neuron* **105**, 837–854 (2020).

11. Keren-Shaul, H. et al. A unique microglia type associated with restricting development of Alzheimer's disease. *Cell* **169**, 1276–1290 (2017).
12. Meilandt, W. J. et al. Trem2 deletion reduces late-stage amyloid plaque accumulation, elevates the Aβ42:Aβ40 ratio, and exacerbates axonal dystrophy and dendritic spine loss in the PS2APP Alzheimer's mouse model. *J. Neurosci.* **40**, 1956–1974 (2020).
13. Bosch-Queralt, M. et al. Diet-dependent regulation of TGFβ impairs reparative innate immune responses after demyelination. *Nat. Metab.* **3**, 211–227 (2021).
14. Dong, Y. et al. Oxidized phosphatidylcholines found in multiple sclerosis lesions mediate neurodegeneration and are neutralized by microglia. *Nat. Neurosci.* **24**, 489–503 (2021).
15. Guerreiro, R. et al. TREM2 variants in Alzheimer's disease. *N. Engl. J. Med.* **368**, 117–127 (2013).
16. Jonsson, T. et al. Variant of TREM2 associated with the risk of Alzheimer's disease. *N. Engl. J. Med.* **368**, 107–116 (2013).
17. Kunkle, B. W. et al. Genetic meta-analysis of diagnosed Alzheimer's disease identifies new risk loci and implicates Aβ, tau, immunity and lipid processing. *Nat. Genet.* **51**, 414–430 (2019).
18. Song, W. et al. Alzheimer's disease-associated TREM2 variants exhibit either decreased or increased ligand-dependent activation. *Alzheimers Dement.* **13**, 381–387 (2017).
19. Bis, J. C. et al. Whole exome sequencing study identifies novel rare and common Alzheimer's-associated variants involved in immune response and transcriptional regulation. *Mol. Psychiatry* **25**, 1859–1875 (2020).
20. Schlepckow, K. et al. An Alzheimer-associated TREM2 variant occurs at the ADAM cleavage site and affects shedding and phagocytic function. *EMBO Mol. Med.* **9**, 1356–1365 (2017).
21. Thornton, P. et al. TREM2 shedding by cleavage at the H157-S158 bond is accelerated for the Alzheimer's disease-associated H157Y variant. *EMBO Mol. Med.* **9**, 1366–1378 (2017).
22. Sims, R. et al. Rare coding variants in *PLCG2*, *ABI3*, and *TREM2* implicate microglial-mediated innate immunity in Alzheimer's disease. *Nat. Genet.* **49**, 1373–1384 (2017).
23. Magno, L. et al. Alzheimer's disease phospholipase C-gamma-2 (PLCG2) protective variant is a functional hypermorph. *Alzheimers Res. Ther.* **11**, 16 (2019).
24. Takalo, M. et al. The Alzheimer's disease-associated protective Plcγ2-P522R variant promotes immune functions. *Mol. Neurodegener.* **15**, 52 (2020).
25. Andreone, B. J. et al. Alzheimer's-associated PLCγ2 is a signaling node required for both TREM2 function and the inflammatory response in human microglia. *Nat. Neurosci.* **23**, 927–938 (2020).
26. Ewers, M. et al. Increased soluble TREM2 in cerebrospinal fluid is associated with reduced cognitive and clinical decline in Alzheimer's disease. *Sci. Transl. Med.* **11**, eaav6221 (2019).
27. Morenas-Rodriguez, E. et al. Soluble TREM2 in CSF and its association with other biomarkers and cognition in autosomal-dominant Alzheimer's disease: a longitudinal observational study. *Lancet Neurol.* **21**, 329–341 (2022).
28. Cheng, Q. et al. TREM2-activating antibodies abrogate the negative pleiotropic effects of the Alzheimer's disease variant *Trem2*^{R47H} on murine myeloid cell function. *J. Biol. Chem.* **293**, 12620–12633 (2018).
29. Cignarella, F. et al. TREM2 activation on microglia promotes myelin debris clearance and remyelination in a model of multiple sclerosis. *Acta Neuropathol.* **140**, 513–534 (2020).
30. Price, B. R. et al. Therapeutic Trem2 activation ameliorates amyloid-beta deposition and improves cognition in the 5×FAD model of amyloid deposition. *J. Neuroinflammation* **17**, 238 (2020).
31. Schlepckow, K. et al. Enhancing protective microglial activities with a dual function TREM2 antibody to the stalk region. *EMBO Mol. Med.* **12**, e11227 (2020).
32. Wang, S. et al. Anti-human TREM2 induces microglia proliferation and reduces pathology in an Alzheimer's disease model. *J. Exp. Med.* **217**, e20200785 (2020).
33. Ellwanger, D. C. et al. Prior activation state shapes the microglia response to antihuman TREM2 in a mouse model of Alzheimer's disease. *Proc. Natl Acad. Sci. USA* **118**, e2017742118 (2021).
34. Fassler, M., Rappaport, M. S., Cuno, C. B. & George, J. Engagement of TREM2 by a novel monoclonal antibody induces activation of microglia and improves cognitive function in Alzheimer's disease models. *J. Neuroinflammation* **18**, 19 (2021).
35. Kariolis, M. S. et al. Brain delivery of therapeutic proteins using an Fc fragment blood–brain barrier transport vehicle in mice and monkeys. *Sci. Transl. Med.* **12**, eaay1359 (2020).
36. Logan, T. et al. Rescue of a lysosomal storage disorder caused by *Grn* loss of function with a brain penetrant progranulin biologic. *Cell* **184**, 4651–4668 (2021).
37. Arguello, A. et al. Molecular architecture determines brain delivery of a transferrin receptor-targeted lysosomal enzyme. *J. Exp. Med.* **219**, e20211057 (2022).
38. Xia, D. et al. Novel *App* knock-in mouse model shows key features of amyloid pathology and reveals profound metabolic dysregulation of microglia. *Mol. Neurodegeneration* **17**, 41 (2022).
39. Mathys, H. et al. Temporal tracking of microglia activation in neurodegeneration at single-cell resolution. *Cell Rep.* **21**, 366–380 (2017).
40. Chen, Y. & Colonna, M. Microglia in Alzheimer's disease at single-cell level. Are there common patterns in humans and mice? *J. Exp. Med.* **218**, e20202717 (2021).
41. Chappel, M. S. et al. Identification of the Fc gamma receptor class I binding site in human IgG through the use of recombinant IgG1/IgG2 hybrid and point-mutated antibodies. *Proc. Natl Acad. Sci. USA* **88**, 9036–9040 (1991).
42. Kim, D. I. et al. An improved smaller biotin ligase for BioID proximity labeling. *Mol. Biol. Cell* **27**, 1188–1196 (2016).
43. Abud, E. M. et al. iPSC-derived human microglia-like cells to study neurological diseases. *Neuron* **94**, 278–293 (2017).
44. Elmore, M. R. et al. Colony-stimulating factor 1 receptor signaling is necessary for microglia viability, unmasking a microglia progenitor cell in the adult brain. *Neuron* **82**, 380–397 (2014).
45. Sayed, F. A. et al. AD-linked R47H-*TREM2* mutation induces disease-enhancing microglial states via AKT hyperactivation. *Sci. Transl. Med.* **13**, eabe3947 (2021).
46. Mukai, T. et al. In-vivo evaluation of indium-111-diethyle netriaminepentaacetic acid-labelling for determining the sites and rates of protein catabolism in mice. *J. Pharm. Pharmacol.* **51**, 15–20 (1999).
47. Cantoni, C. et al. TREM2 regulates microglial cell activation in response to demyelination in vivo. *Acta Neuropathol.* **129**, 429–447 (2015).
48. Olzmann, J. A. & Carvalho, P. Dynamics and functions of lipid droplets. *Nat. Rev. Mol. Cell Biol.* **20**, 137–155 (2019).
49. Marschallinger, J. et al. Lipid-droplet-accumulating microglia represent a dysfunctional and proinflammatory state in the aging brain. *Nat. Neurosci.* **23**, 194–208 (2020).
50. Loving, B. A. & Bruce, K. D. Lipid and lipoprotein metabolism in microglia. *Front. Physiol.* **11**, 393 (2020).
51. Liesa, M. & Shirihai, O. S. Mitochondrial dynamics in the regulation of nutrient utilization and energy expenditure. *Cell Metab.* **17**, 491–506 (2013).
52. Rambold, A. S. & Pearce, E. L. Mitochondrial dynamics at the interface of immune cell metabolism and function. *Trends Immunol.* **39**, 6–18 (2018).

53. Oakley, H. et al. Intraneuronal β-amyloid aggregates, neurodegeneration, and neuron loss in transgenic mice with five familial Alzheimer's disease mutations: potential factors in amyloid plaque formation. *J. Neurosci.* **26**, 10129–10140 (2006).
54. Xiang, X. et al. Microglial activation states drive glucose uptake and FDG-PET alterations in neurodegenerative diseases. *Sci. Transl. Med.* **13**, eabe5640 (2021).
55. Kleinberger, G. et al. The FTD-like syndrome causing TREM2 T66M mutation impairs microglia function, brain perfusion, and glucose metabolism. *EMBO J.* **36**, 1837–1853 (2017).
56. Gotzl, J. K. et al. Opposite microglial activation stages upon loss of PGRN or TREM2 result in reduced cerebral glucose metabolism. *EMBO Mol. Med.* **11**, e9711 (2019).
57. Jack, C. R. Jr. et al. Tracking pathophysiological processes in Alzheimer's disease: an updated hypothetical model of dynamic biomarkers. *Lancet Neurol.* **12**, 207–216 (2013).
58. Ou, Y. N. et al. FDG-PET as an independent biomarker for Alzheimer's biological diagnosis: a longitudinal study. *Alzheimers Res. Ther.* **11**, 57 (2019).
59. Wang, Y. et al. TREM2 ameliorates neuroinflammatory response and cognitive impairment via PI3K/AKT/FoxO3a signaling pathway in Alzheimer's disease mice. *Aging (Albany NY)* **12**, 20862–20879 (2020).
60. Ullman, J. C. et al. Brain delivery and activity of a lysosomal enzyme using a blood–brain barrier transport vehicle in mice. *Sci. Transl. Med.* **12**, eaay1163 (2020).
61. Reifschneider, A. et al. Loss of TREM2 rescues hyperactivation of microglia, but not lysosomal deficits and neurotoxicity in models of progranulin deficiency. *EMBO J.* **41**, e109108 (2022).
62. Piers, T. M. et al. A locked immunometabolic switch underlies TREM2 R47H loss of function in human iPSC-derived microglia. *FASEB J.* **34**, 2436–2450 (2020).
63. Ulland, T. K. et al. TREM2 maintains microglial metabolic fitness in Alzheimer's disease. *Cell* **170**, 649–663 (2017).

Bettina van Lengerich[1,8], Lihong Zhan[1,8], Dan Xia[1,8], Darren Chan[1], David Joy[1], Joshua I. Park[1], David Tatarakis[1], Meredith Calvert[1], Selina Hummel[2,3], Steve Lianoglou[1], Michelle E. Pizzo[1], Rachel Prorok[1], Elliot Thomsen[1], Laura M. Bartos[3], Philipp Beumers[3], Anja Capell[4], Sonnet S. Davis[1], Lis de Weerd[2], Jason C. Dugas[1], Joseph Duque[1], Timothy Earr[1], Kapil Gadkar[1], Tina Giese[1], Audrey Gill[1], Johannes Gnörich[3], Connie Ha[1], Malavika Kannuswamy[1], Do Jin Kim[1], Sebastian T. Kunte[3], Lea H. Kunze[2,3], Diana Lac[1], Kendra Lechtenberg[1], Amy Wing-Sze Leung[1], Chun-Chi Liang[1], Isabel Lopez[1], Paul McQuade[5], Anuja Modi[1], Vanessa O. Torres[1], Hoang N. Nguyen[1], Ida Pesämaa[2,6], Nicholas Propson[1], Marvin Reich[2,6], Yaneth Robles-Colmenares[1], Kai Schlepckow[2], Luna Slemann[3], Hilda Solanoy[1], Jung H. Suh[1], Robert G. Thorne[1], Chandler Vieira[1], Karin Wind-Mark[2,3], Ken Xiong[1], Y. Joy Yu Zuchero[1], Dolo Diaz[1], Mark S. Dennis[1], Fen Huang[1], Kimberly Scearce-Levie[1], Ryan J. Watts[1], Christian Haass[2,4,7], Joseph W. Lewcock[1], Gilbert Di Paolo[1], Matthias Brendel[2,3,7], Pascal E. Sanchez[1] ✉ & Kathryn M. Monroe[1] ✉

[1]Denali Therapeutics, Inc., South San Francisco, CA, USA. [2]German Center for Neurodegenerative Diseases (DZNE), Munich, Germany. [3]Department of Nuclear Medicine, University Hospital of Munich, Ludwig Maximilians University, Munich, Germany. [4]Biomedical Center (BMC), Division of Metabolic Biochemistry, Faculty of Medicine, Ludwig Maximilians University, Munich, Germany. [5]Takeda Pharmaceutical Company, Cambridge, MA, USA. [6]Graduate School of Systemic Neurosciences, Ludwig Maximilians University Munich, Planegg-Martinsried, Germany. [7]Munich Cluster for Systems Neurology (SyNergy), Munich, Germany. [8]These authors contributed equally: Bettina van Lengerich, Lihong Zhan, Dan Xia. ✉e-mail: sanchez@dnli.com; monroe@dnli.com

Methods

Mouse lines and animal care

The genotype, age and sex information of mouse models used in this study are summarized in Supplementary Table 2. TfR$^{mu/hu}$ mouse line was developed in-house by humanizing the apical domain of mouse TfR[35,36]. The chimeric allele is referred to as TfR$^{mu/hu}$. *App^{SAA}* mouse model[38] was crossed to TfR$^{mu/hu}$ mice to generate *App*^{SAA};TfR$^{mu/hu}$ mice (homozygous;homozygous). The human Trem2 BAC tg mouse model was generated at Denali Therapeutics by the introduction of engineered BAC DNA CTD-2210D2 into the mouse genome (see the detailed description in the Supplementary Methods). 5×FAD mice (B6SJLTg(APP SwFlLon,PSEN1*M146L*L286V)6799Vas/Mmjax) were purchased from the Jackson Laboratory (MMRRC strain no. 034840-JAX)[53]. 5×FAD mice, human TREM2 BAC tg mice and TfR$^{mu/hu}$ mice were crossed to generate 5×FAD;hTREM2 tg;TfR$^{mu/hu}$ (hemizygous;hemizygous;homozygous) and WT;hTREM2 tg;TfR$^{mu/hu}$ mice (non-carrier;hemizygous;homozygous). Mice are maintained on a C57BL/6J genetic background. Mouse husbandry and experimental procedures were approved by the Denali Institutional Animal Care and Use Committee. All animal experiments at the German Center for Neurodegenerative Diseases (DZNE) were performed in accordance with animal handling laws of the state of Bavaria (Germany). Housing conditions included standard pellet food and water provided ad libitum, a 12-hour light/dark cycle at a temperature of 22 °C with maximal five mice per cage and cage replacement once per week with regular health monitoring.

RNA-seq

iMG RNA was extracted with the RNeasy Plus Micro Kit (Qiagen, 74034) to be used as input for bulk RNA-seq library generation using the Quant-Seq 3′ mRNA-seq Library Prep Kit FWD for Illumina (Lexogen, A01173) with the unique molecular identifier (UMI) second-strand synthesis add-on module. Libraries were pooled and shipped to SeqMatic for sequencing on an Illumina sequencer.

scRNA-seq for WT mice was prepared with the Miltenyi Adult Brain Dissociation Kit (Miltenyi Biotec, 130-107-677), followed by enrichment with CD45 micro beads (Miltenyi Biotec, 130-107-677). 10x Genomics Chromium Single Cell 3′ GEM, Library & Gel Bead Kit version 3, was used for single-cell capture and library generation per the user guide. Samples for the AD mouse model were prepared with the same Miltenyi dissociation kit, but enrichment was performed via FACS sorting of live CD11b$^+$ cells. Samples were labeled with CellPlex reagents for multiplexing purposes, and single-cell capture was performed using the Chromium Next GEM Single Cell 3′ Kit version 3.1 per the user guide. Detailed information for bulk and scRNA-seq experimental procedures can be found in the Supplementary Methods section.

Raw reads were aligned to the mouse genome (mm10) using STAR aligner[64]. For scRNA-seq, reads were mapped using the standard Cell Ranger pipeline (version 6.1.1/version 7.0.0). Downstream analysis of bulk RNA-seq data was carried out in R. Differential expression was performed using the limma/voom pipelines[65]. GSEA was performed with the fgsea[66] and sparrow (https://github.com/lianos/sparrow) packages using signatures from the hallmark Molecular Signatures Database (MSigDB)[67,68]. For scRNA-seq, analyses were performed in R using the standard Seurat version 4 pipeline[69]. Pseudobulk differential expression analyses were carried out using limma/voom. Detailed information about processing and analysis steps can be found in the Supplementary Methods; for analysis code, see the ‘Code availability’ section.

IHC for mouse brains

After cardiac perfusion with ice-cold PBS, right hemibrains were fixed by immersion in 4% paraformaldehyde (PFA) at 4 °C for 24 hours and then transferred to 30% sucrose solution for 2 days before sectioning coronally on a freezing microtome at a thickness of 40 µm. Free-floating sections were permeabilized with 1× Tris-buffered saline solution containing 0.05% Tween (TBST), blocked with 5% donkey serum and incubated in primary antibodies overnight at 4 °C. Sections were then washed in TBST, and a solution of secondary antibodies was then applied for 1 hour at room temperature. Sections were washed in TBST before mounting and cover-slipping with ProLong Glass Antifade Mountant solution (Thermo Fisher Scientific, P36984). Immunofluorescence was performed using the following primary antibodies: goat anti-Iba1 (Novus, NB100-1028, 1:500); guinea pig anti-Iba1 (Synpatic Systems, HS-234 308, 1:500); rabbit anti-CD74 (Abcam, ab245692, 1:500); and goat anti-Axl (R&D Systems, AF854, 1:25) and the following secondary antibodies: Alexa Fluor 488 donkey anti-Rabbit IgG (Jackson ImmunoResearch, 711-545-152, 1:500); Alexa Fluor 555 donkey anti-rabbit IgG (Thermo Fisher Scientific, A32794, 1:500); Alexa Fluor 647 donkey anti-goat IgG (Thermo Fisher Scientific, A-21447, 1:500); and Alexa Fluor 647 donkey anti-guinea pig IgG (Jackson ImmunoResearch, 706-605-148, 1:500). To quantify microglia coverage in the brains, immunohistochemical staining by DAB precipitation coloring was also performed after goat anti-Iba1 primary incubation. The sections with immunofluorescence staining were imaged and analyzed for microglia morphology. See Supplementary Methods for details on microglia morphology quantification.

Detection of antibody concentrations

Antibody concentrations were quantified using a generic anti-human IgG sandwich-format ELISA. Plates were coated overnight at 4 °C with donkey anti-human IgG (Jackson ImmunoResearch, 709-006-098) at 1 µg ml^{-1} in sodium bicarbonate solution (Sigma-Aldrich, C3041-50CAP) with gentle agitation. Plates were washed 3× with PBS + 0.05% Tween 20. Assay standards and samples were diluted in PBS + 0.05% Tween 20 + 1% BSA (10 mg ml^{-1}). A standard curve ranging from 0.41 ng ml^{-1} to 1,500 ng ml^{-1} (0.003–10 nM) was fitted using a four-parameter logistic regression. Standards and diluted samples were incubated with agitation for 2 hours at room temperature. Plates were washed 3×. Detection antibody, HRP-conjugated goat anti-human IgG (Jackson ImmunoResearch, 109-036-098), was diluted in blocking buffer (PBS + 0.05% Tween 20 + 5% BSA (50 mg ml^{-1})) to a final concentration of 0.02 µg ml^{-1}, and plates were incubated with agitation for 1 hour at room temperature. After a final 3× wash, plates were developed by adding TMB substrate for 5–10 minutes. Reaction was quenched by adding 4N H_2SO_4. Absorbance at 450 nm was measured.

In vivo detection of mouse microglial proliferation

Animals were dosed with EdU solution (20 mg ml^{-1}, Santa Cruz Biotechnology, sc-284628) via intraperitoneal (IP) injection at 80 mg kg^{-1} at day 0 (30 minutes after antibody treatment), then at 1, 2, and 3 days. Four days after EdU injection, animals were deeply anesthetized via IP injection of 2.5% Avertin. The mice were then perfused intracardially with cold PBS. Left hemibrain was snap-frozen on dry ice for biochemical analysis. Right hemibrain was fixed in 4% PFA at 4 °C for 24 hours for sectioning and immunostaining. For detecting EdU$^+$ microglia in brain sections, Click-iT EdU imaging kits (Thermo Fisher Scientific, C10637) were used following the manufacturer’s instructions before the Iba1 immunofluorescence staining procedures.

Generation of TREM2-DAP12 overexpression HEK293 stable cell lines

Human TREM2/DAP12 is overexpressed in HEK293 cell line (RRID: CVCL_0045, ATCC: PTA-4488) by transfection of a dual promoter pBudCE4.1 vector driving expression of TREM2 under the CMV promoter and DAP12 the under the EF1a promoter.

Stable clones were isolated after zeocin selection (800 µg ml^{-1} for 10 days), and TREM2 was detected by flow cytometry (APC-conjugated rat anti-human/mouse-TREM2 monoclonal antibody, R&D Systems, MAB17291). The clone showing the highest TREM2 expression level was selected.

pSyk signaling

Phospho-Syk was measured by the AlphaLISA assay following the manufacturer's protocol (PerkinElmer, ALSU-PSYK-A10K). In brief, hTREM2-DAP12 HEK293 cells were plated at 50,000 cells per well the day before the assay. Cells are stimulated with TREM2 antibodies for 5 minutes at 37 °C using Bravo liquid handler. For the TfR blocking experiment, TREM2 antibody was mixed with a custom-made monoclonal TfR antibody that binds the ATV epitope in the apical domain (K_D ~0.9 nM) at 37 °C for 30 minutes before adding to the cells. Cells are lysed with lysis buffering containing 1 μM PMSF. Data are collected from PerkinElmer EnVision plate reader.

IP assay

hTREM2-DAP12 HEK293 cells were plated on 10-cm dishes coated with PDL 24 hours before antibody treatment. Cell lysate was collected with 1-ml ice-cold IP buffer (Thermo Fisher Scientific, 87787) containing 1× protease inhibitor (Cell Signaling Technology, 5872) using a cell scraper. Cell lysate was normalized based on BCA measurement. Then, 200–400 μg of total lysate was used for each IP and was mixed with 2 μg of biotinylated capturing antibody at 4 °C overnight. Normal IgG from the same species as the IP capturing antibody was used as binding control. Antibody biotinylation was performed using an EZ-Link Sulfo-NHS-LC-Biotin Kit, following the manufacturer's instructions (Thermo Fisher Scientific, A39257). For TREM2 IP, goat anti-TREM2 antibody (R&D Systems, AF1828) and normal goat IgG (R&D Systems, AB-108-C) was used as capturing antibody. For the reciprocal TfR IP, a human monoclonal clonal antibody against TfR and an isotype IgG isotype antibody were made in-house for the study. The immune complex was then precipitated using 20 μl of streptavidin-conjugated magnetic beads (Resyn Biosciences, MR-STV005) and washed 4× with ice-cold 1× PBS buffer containing 0.05% Tween 20. For protein elution, 25 μl of LDS containing 1× sample buffer (Thermo Fisher Scientific, NP0007) and 1× reducing agent (Thermo Fisher Scientific, NP0009) was added directly to the washed beads and incubated at 75 °C for 10 minutes. Samples were then analyzed following standard western blot protocol. The following antibodies were used for western detection: anti-TREM2 (R&D Systems, AF1828), anti-TfR (Thermo Fisher Scientific, 13-6800) and anti-actin (Cell Signaling Technology, 58169S).

BioID-based antibody clustering assay

TREM2 fusion protein tagged with BioID2, a mini biotin ligase[42], was cloned into the pLVX-TRE3G vector (Takara, 631187) using In-Fusion reagent (Takara, 638943). To further optimize the catalytic activity of BioID2, four additional point mutations (E62R, q68g, p70g and S112A) were added to the sequence as previously described[70]. The pLVX-TRE3G-TREM2-BioID2 plasmid and the transponder pLVX-EF1a-Tet3G plasmid (Takara, 631359) were introduced into the parental hTREM2-DAP12 HEK293 cells as stable cell line. Cells were maintained in biotin-free media containing DMEM (Gibco, 11965092), 10% dialyzed FBS (R&D Systems, S12850), 1× NEAA (Gibco, 11140-050), 1× sodium pyruvate (Gibco, 11360-070) and 1× P/S (Gibco, 15140-122). Twenty-four hours before the assay, 2–4 ng ml^{-1} of Dox was added to initiate TREM2-BioID fusion protein expression. Cells were treated with antibody solution containing 100 nM TREM2 antibody and 2 μM biotin prepared in 1× PBS for 10 minutes at 37 °C. Both no-Dox and no-biotin samples were included as negative control. Cell lysates were prepared with RIPA buffer (Teknova, R3792) containing 1× phosphatase/protease inhibitor (Cell Signaling Technology, 5872). Normalized protein lysate containing 0.5–1 mg of protein was incubated with 20 μl of magnetic streptavidin beads (Resyn Biosciences, MR-STV005) at 4 °C overnight. Beads were then washed 4× with ice-cold RIPA buffer. Captured protein was eluted with 2× NuPAGE LDS sample buffer (Thermo Fisher Scientific, NP0007) supplied with additional 1% SDS, 20 mM biotin and 1× reducing agent (Thermo Fisher Scientific, NP0009) and heated at 95 °C for 10 minutes. Samples were analyzed via western blot. Goat anti-TREM2 (R&D Systems, AF1828) and anti-goat HRP secondary antibody (Thermo Fisher Scientific, 81-1620) were used for detection with ECL reagent (Bio-Rad, 1705060). For quantification, TREM2 biotinylation near 28 K_D was normalized to the auto-biotinylation of TREM2-BioID band above 55 K_D.

TREM2 receptor and ATV:TREM2 trafficking endosomal signaling by immunofluorescence microscopy

Human hTREM2-DAP12 HEK293 cells were plated at 35,000 cells per well 1 day before the experiment. Cells were starved in serum-free DMEM for 1 hour before antibody stimulation at 10 nM and 37 °C for 10 minutes. Transferrin is labeled with Alexa Fluor 647 transferrin conjugate (Invitrogen, T23366) at 20 μg ml^{-1} during antibody stimulation. Cells were fixed in 4% PFA for 10 minutes and permeabilized/blocked in PBS containing 0.3% Triton and 5% BSA. Primary antibodies were diluted (1:250) in PBST buffer (0.06% Triton and 1% BSA in PBS) and used at 4 °C for 24 hours with anti-pSyk Tyr525/526 (Cell Signaling, 2711) and anti-EEA1 (BD Biosciences, 610456). Secondary antibodies were diluted (1:500) in PBST buffer and used at room temperature for 45 minutes with Alexa Fluor 488 anti-human IgG (Jackson ImmunoResearch, 109-545-003); Alexa Fluor 568 anti-rabbit (Thermo Fisher Scientific, A10042); and Alexa Fluor 647 anti-mouse (Thermo Fisher Scientific, A31572). Cells were washed with PBS 3× between each stain.

Data were acquired with Opera Phoenix High-Content Imager (PerkinElmer) at ×63 magnification. Image quantification was performed using Harmony software (PerkinElmer, version 5.1) with spot identification algorithm to quantify the fluorescence spot intensity by channel. A masking algorithm was implemented in Harmony software to quantify the percent of IgG or pSyk spots co-localized within EEA1 or TfR.

Western blot detection of signaling pathway activation in iMG

Cell lysates were prepared in high-salt lysis buffer (Cell Signaling Technology, 9803) with protease and phosphatase inhibitors (Cell Signaling Technology, 5872). BCA assay (Thermo Fisher Scientific, 23225) was used to measure total protein. Normalized lysates were mixed with loading buffer (Thermo Fisher Scientific, NP0007) and reducing agent (Thermo Fisher Scientific, NP0004) and then resolved by electrophoresis using 4–12% NuPAGE (Thermo Fisher Scientific, NP0335BOX). Semi-dry transfer was performed using the Trans-Blot Turbo System (Bio-Rad, 1704150) with 0.2-μm PVDF transfer packs (Bio-Rad, 17001917). Transferred blots were blocked with Intercept Blocking Buffer (LI-COR, 927-60001) and incubated with primary antibody overnight. HRP-conjugated secondary antibodies were used for detection. Washes were performed using TBST buffer containing 0.05% Tween 20. Blots were developed using ECL reagent (Bio-Rad, 1705062) and imaged by the Li-COR Odyssey Fc imaging system. Band signal intensity was quantified using Image Studio Lite software (LI-COR, version 5.2.5).

Table of Western blot antibody reagents.

Antibody	Source	Cat.	Dilution
mTOR (7C10)	CST	2983T	1:500
Phospho-mTOR (Ser2448)	CST	5536T	1:500
AKT (C67E7)	CST	4691T	1:500
Phospho-Akt (Ser473)	CST	9271T	1:250
Phospho-RPS6 (Ser235/236)	CST	4858T	1:500
Phospho-GSK-3β (Ser9)	CST	5558T	1:500
β-actin (E4D9Z)	CST	58169S	1:1,000
Phospho-4E-BP1 (Thr37/46)	CST	2855T	1:250
Phospho-Erk1/2 (Thr202/Tyr204)	CST	4370S	1:1,000
Anti-rabbit HRP 2nd antibody	CST	7074S	1:2,000
Anti-mouse HRP 2nd antibody	CST	7076P2	1:2,000

iMG proliferation assay

iMG were plated in cell carrier ultra 96-well plate (PerkinElmer, 6055302) at a density of 25,000 cells per well and equilibrated for 72 hours in IMDM media (Thermo Fisher Scientific, 12440061) containing 10% FBS (Hyclone, SH30071.03), 20 ng ml^{-1} of granulocyte-macrophage colony-stimulating factor (GM-CSF), 20 ng ml^{-1} of IL-3 and 20 ng ml^{-1} of M-CSF. Cells were dosed with 100 nM antibody prepared in reduced cytokine media containing 10% FBS (Cytiva, SH30071.03), 5 ng ml^{-1} of GM-CSF, 5 ng ml^{-1} of IL-34 and 5 ng ml^{-1} of CSF1. Twenty nM mTOR kinase inhibitor AZD8055 (AZD, Selleck Chemicals, S1555) was dosed with antibody. Forty-eight hours after treatment, 20 µM EdU was added, and cells were treated for 96 hours before being fixed by 4% PFA at room temperature for 10 minutes and stained with EdU labeling kit (Thermo Fisher Scientific, C10637), DAPI (Thermo Fisher Scientific, 62248) and cell mask (Thermo Fisher Scientific, H32721). Fluorescent images were collected on Opera Phenix High-Content Imaging system equipped with a ×20 water lens (NA = 1.0). A total of nine fields per well were collected using three-step z-planes separated by 2 µm. Total cell count was measured by counting DAPI$^+$ nuclei using the 'find nuclei' function of Harmony software (PerkinElmer, version 4.9). EdU$^+$ nuclei were quantified from the 488 channel, and frequency was calculated by normalizing to total DAPI$^+$ nuclei.

CSF1R detection assay

CSF1R levels in brain homogenates and CSF were quantified using a commercial ELISA assay (Abcam, ab240681). Brain homogenates were diluted 40-fold, and CSF was diluted 50-fold in NS diluent buffer supplied from the kit. Samples were assessed in duplicate wells, and the average reading was taken as the CSF1R protein level for that sample.

Ex vivo phagocytosis assay

Mice were taken down 2 days after antibody dosing, and brains were dissected after PBS perfusion and dissociated with the Adult Brain Dissociation Kit (Miltenyi Biotec, 130-107-677), according to the manufacturer's protocol. Microglia number was measured by FACS using CountBright Absolute Counting Beads (Invitrogen, C36950) and diluted to 500 microglia per µl in DPBS + 0.5% BSA. The resulting cell suspension was mixed with pHrodo-green labeled myelin (50 µg ml^{-1} in DPBS + 0.5% BSA) or FAM-Aβ (200 nM in DPBS + 0.5% BSA) and incubated at 37 °C for 45 minutes with gentle mixing. Cell suspensions were washed and stained with the following antibodies in FACS buffer (1% fatty acid-free BSA and 1 mM EDTA in PBS) for 25 minutes on ice: CD11b-BV421 (BioLegend, 101251) and mouse Fc blocker (anti-mouse CD16/32, BioLegend, 101320). Cells were washed with FACS buffer, resuspended in FACS buffer with propidium iodide (Miltenyi Biotec, 130-93-233), strained through a 100-µm filter and then analyzed on a flow cytometer (BD FACSAria III). FCS files were then imported and analyzed in FlowJo software (version 10).The percentage of myelin$^+$ microglia (pHrodo-green$^+$, CD11b$^+$) and Aβ$^+$ microglia (FAM$^+$, CD11b$^+$) in the total CD11b$^+$ microglial population was calculated. See Supplementary Methods for details on myelin debris and Aβ fibril preparation and fluorescent labeling.

In vitro iMG lipid storage assay

iMG (30,000 cells per well) were plated on PDL-coated 96-well plates in microglia differentiation media. After 24 hours at 37 °C, media containing 15 µg ml^{-1} of purified unlabeled myelin[71] was added (see Supplementary Methods for details). After 24 hours at 37 °C, media was exchanged for media containing 100 nM ATV:TREM2 or ATV:ISO antibody and incubated for another 48 hours at 37 °C before imaging BODIPY staining or lipidomics extractions. For BODIPY imaging, cells were incubated at 37 °C for 30 minutes in live cell imaging buffer (Life Technologies, A14291DJ) containing 1 µM BODIPY 493/503 (Thermo Fisher Scientific, D3922) and 1 drop per milliliter of NucBlue (Thermo Fisher Scientific, R37605). Cells were fixed in 4% PFA and imaged using Alexa Fluor 488 and DAPI on an Opera Phenix High-Content confocal imager. Lipid spots were analyzed using a spot-finding algorithm on Harmony software.

For lipidomic analysis, cells were washed once with PBS on ice. Then, 100 µl of a 9:1 methanol:water solution containing 2 µl of internal standard mixture was added to the cells. The plate was agitated on a shaker at 4 °C and 1,200 r.p.m. for 20 minutes and centrifuged for 5 minutes at 300*g*. A sample of supernatant was transferred to LC–MS vials and kept at −80 °C. See Supplementary Methods for details LC–MS analysis.

Seahorse detection of cellular respiration

iMG (20,000 cells per well) were seeded on a PDL-coated 96-well Agilent Seahorse XF Cell Culture microplate in media. For the fatty acid oxidation studies, 3 days before assay, media replaced with substrate-limited media comprised of XF DMEM, 1% FBS, 0.5 mM glucose, 1 mM glutamine and 0.5 mM carnitine. Antibodies were added to cells for a final concentration of 100 nM and incubated for 3 days. Cells were washed twice, and antibody was re-added to the washed cells to a final concentration of 100 nM. Cells were imaged using bright-field microscopy to obtain cell counts for normalization. Cells were then incubated for 1 hour in a non-CO_2 incubator. Ports on the sensor plate were filled according to the XF Long Chain Fatty Acid Oxidation Stress Kit or XF Glucose Oxidation Kit, and cells were subjected to sequential injections of oligomycin (final concentration 1.5 µM), FCCP (2-[2-[4-(trifluoromethoxy)phenyl] hydrazinylidene]-propanedinitrile) (2 µM for fatty acid oxidation and 1.5 µM for glucose oxidation) and rotenone/antimycin A (0.5 µM each). In experiments using inhibitors, etomoxir or UK5099 were added in port A at 4 µM or 3 µM, respectively. Data were analyzed using the Agilent Seahorse Analytics online software to generate kinetic curves and calculate maximal respiration and spare capacity.

PET imaging study

On day 0, 5–6-month-old WT;hTREM2 tg;TfR$^{mu/hu}$ mice and 4.5-months-old 5×FAD;hTREM2 tg;TfR$^{mu/hu}$ mice ($n = 6$ each) were IP injected with ATV:TREM2 or an isotype control antibody at 14 mg kg^{-1} and 10 mg kg^{-1}, respectively. Mice were subjected to either TSPO-PET or FDG-PET imaging 24 hours after dose. Microglia activation and brain glucose metabolism were followed longitudinally with further PET scans on days 4 and 8 after antibody administration. Male and female mice were distributed evenly among both antibody treatment and PET imaging groups. See Supplementary Methods for details on PET imaging procedures and quantification.

Statistics and reproducibility

All statistical analyses were run in GraphPad Prism 9 or R Studio (version 1.4.1717). Data are presented as mean ± s.e.m. with raw dot plots. The number of animals, cells, imaging fields, experiment replicates and statistical tests are indicated in the figure legends. All in vitro data are from at least three independent experiments. The samples were not blinded during initial study planning to ensure that the number of groups of mice were randomized and balanced, and age and sex were matched. RNA-seq datasets were not blinded for analysis. Image analysis and ex vivo assays were performed in a blinded fashion. In vitro studies were performed unblinded. The PET imaging analysis was not blinded; however, we used an automated pipeline[72,73] such that the operator cannot influence/bias the results because the co-registration and the voi extraction is a defined procedure.

All statistical analyses performed were two-tailed. Data normality was examined by the Shapiro–Wilk test. *F*-test or Brown–Forsythe test was used to assess data homoscedasticity. If data meet statistical assumptions, unpaired *t*-test, paired *t*-test, Dunnett's multiple comparisons test, Tukey's multiple comparisons test or multiple *t*-test was used depending on data groups. For non-parametric statistics, unpaired *t*-test with Welch's correction test or Kruskal–Wallis test was used.

Data with normal distribution but unequal variance were assessed with Mann–Whitney test or Brown–Forsythe and Welch's ANOVA test. Statistical *P* values are shown on graphs denoted with '*P* = '.

Reporting summary

Further information on research design is available in the Nature Portfolio Reporting Summary linked to this article.

Data availability

The raw and processed bulk/scRNA-seq data have been deposited in the National Center for Biotechnology Information's Gene Expression Omnibus (GEO) and are accessible through GEO SuperSeries accession number GSE200276. This SuperSeries is composed of three individual series: GSE199154, GSE198987 and GSE200275. Raw and processed files for the AD model scRNA-seq study are accessible through GEO accession number GSE209912.

The metabolomics data were uploaded to the MetaboLights repository with study ID MTBLS6543. Source data are provided with this paper.

Code availability

All R and Python code used to produce transcriptomics analyses and imaging morphometric analyses are available through GitHub at the following URL: https://github.com/denalitherapeutics/Lengerich_natneuro_2022.

References

64. Dobin, A. et al. STAR: ultrafast universal RNA-seq aligner. *Bioinformatics* **29**, 15–21 (2013).
65. Ritchie, M. E. et al. limma powers differential expression analyses for RNA-sequencing and microarray studies. *Nucleic Acids Res.* **43**, e47 (2015).
66. Korotkevich, G. et al. Fast gene set enrichment analysis. Preprint at https://www.biorxiv.org/content/10.1101/060012v3 (2021).
67. Subramanian, A. et al. Gene set enrichment analysis: a knowledge-based approach for interpreting genome-wide expression profiles. *Proc. Natl Acad. Sci. USA* **102**, 15545–15550 (2005).
68. Liberzon, A. et al. The Molecular Signatures Database (MSigDB) hallmark gene set collection. *Cell Syst.* **1**, 417–425 (2015).
69. Hao, Y. et al. Integrated analysis of multimodal single-cell data. *Cell* **184**, 3573–3587 (2021).
70. Branon, T. C. et al. Efficient proximity labeling in living cells and organisms with TurboID. *Nat. Biotechnol.* **36**, 880–887 (2018).
71. Safaiyan, S. et al. Age-related myelin degradation burdens the clearance function of microglia during aging. *Nat. Neurosci.* **19**, 995–998 (2016).
72. Overhoff, F. et al. Automated spatial brain normalization and hindbrain white matter reference tissue give improved [^{18}F]-florbetaben PET quantitation in Alzheimer's model mice. *Front. Neurosci.* **10**, 45 (2016).
73. Brendel, M. et al. Glial activation and glucose metabolism in a transgenic amyloid mouse model: a triple-tracer PET study. *J. Nucl. Med.* **57**, 954–960 (2016).

Acknowledgements

We thank S. Andrews, J. Kessler, Z. Sweeney and S. Weninger for thoughtful discussions. We thank J. Shi, K. Mei, H. Chen and R. Rakhit for their work at the early stage of the project. We thank A. Silverman and L. Shan for guidance on antibody engineering. We thank T. Sandmann for input on RNA sequencing data access. We thank K. Raju for cloning and optimization of the BioID in vitro system. We thank M. Kariolis for the anti-TfR antibody. We thank our collaborators K. Lisaingo, S. Duncan and C. da Roza at AbCellera Biologics, Inc. for antibody discovery.

Author contributions

B.V.L., L.Z., M.S.D., R.J.W., D.X., S.L., P.E.S., C.H., G.D.P., J.W.L. and K.M.M. conceived of the study idea and approaches. B.V.L., L.Z., D.X., S.L., J.I.P., D.J., D.C., K.G., M.C., M.B., L.M.B., S.T.K., F.H., K.S.-L., M.E.P., Y.J.Y.Z., R.G.T., K.L., J.H.S., A.C., S.T.K., L.M.B., M.B., P.M.Q., C.H., G.D.P., P.E.S. and K.M.M. designed experiments. B.V.L., L.Z., D.X., J.I.P., M.C., D.J., S.H., K.W.-M., S.T.K., P.B., L.M.B., J.G., L.H.K., H.N.N., L.S., S.S.D., E.T., L.D.W., M.R., I.P., S.T.K., P.B., L.M.B., J.G., L.H.K., L.S., A.M., R.P., D.J.K., Y.R.-C., J.D., T.G., C.V., N.P., C.-C.L., V.O.T., T.E., I.L., H.S. and J.D. performed experiments. S.L., B.V.L., L.Z., D.X., D.C., K.G., J.I.P., R.P., D.J., D.T., M.C., K.L., P.M.Q., A.M., S.H., S.T.K., P.B., L.M.B., J.G., M.B., A.G. and D.L. analyzed and interpreted data. C.H., K.S.-L., M.C., M.B., S.H., D.D., D.T., G.D.P. and J.W.L. edited the manuscript. B.V.L., L.Z., D.X., D.T., S.L., D.J., K.L., P.E.S. and K.M.M. wrote the manuscript.

Competing interests

All authors, except P.M.Q., S.H., P.B., A.C., J.G., S.T.K., L.H.K., I.P., K.S., L.S., L.D.W., K.W.-M., M.R., L.M.B., M.B. and C.H., are full-time employees and/or shareholders of Denali Therapeutics. C.H. is a collaborator of Denali Therapeutics, participated on one advisory board meeting of Biogen and received a speaker honorarium from Novartis and Roche. C.H. is chief advisor of ISAR Bioscience and a member of the advisory board of AviadoBio. P.M.Q. is a full-time employee of Takeda Pharmaceuticals, Inc., a clinical development partner of Denali Therapeutics. This work has been described, in part, in pending patent applications.

Additional information

Extended data is available for this paper at https://doi.org/10.1038/s41593-022-01240-0.

Supplementary information The online version contains supplementary material available at https://doi.org/10.1038/s41593-022-01240-0.

Correspondence and requests for materials should be addressed to Pascal E. Sanchez or Kathryn M. Monroe.

Peer review information *Nature Neuroscience* thanks Takanori Yokota and the other, anonymous, reviewer(s) for their contribution to the peer review of this work.

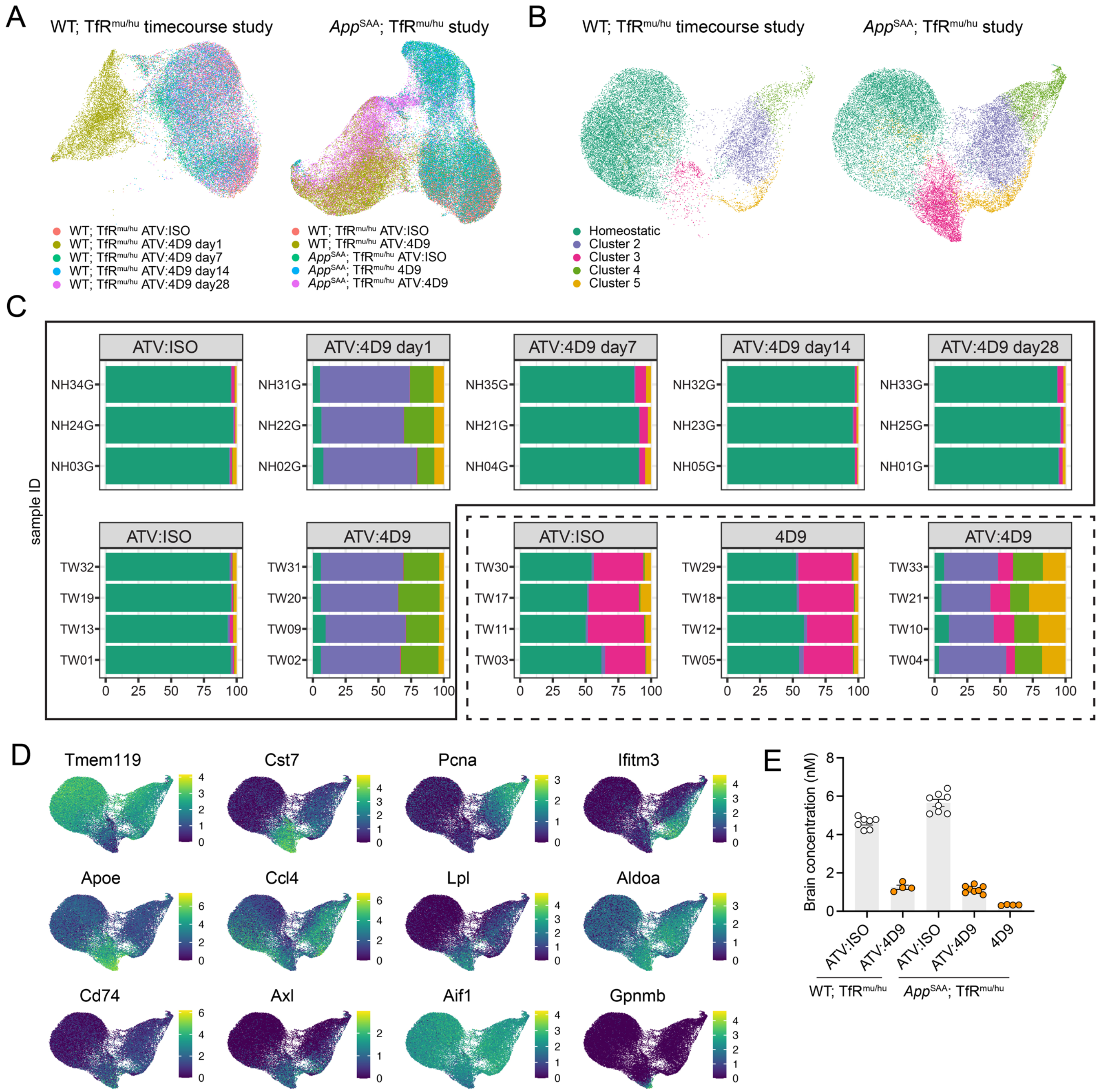

Extended Data Fig. 1 | ATV:4D9 induces temporally dynamic microglial states distinct from amyloid pathology. (a) UMAP projections of individually processed data sets for WT; TfR$^{mu/hu}$ timecourse and TfR$^{mu/hu}$; *App*^{SAA} studies. Microglia are color coded according to their experimental group. **(b)** Combined UMAP of integrated data by study. Microglia are color coded by unbiased cluster assignment. **(c)** Stacked barplots showing the proportion of microglia per biological replicate by cluster. Plots are grouped by experimental group, and each bar represents a biological replicate within that group. Barplot color scheme is consistent with clusters in **b**. **(d)** Feature plots showing expression of selected individual genes. Microglia are color coded according to log normalized expression of each gene. **(e)** Antibody concentrations detected in whole brain lysate from either WT; TfR$^{mu/hu}$ or TfR$^{mu/hu}$; *App*^{SAA} mice dosed with 10 mg kg^{-1} ATV:ISO or ATV:4D9 (n = 8 mice/group, except for ATV:4D9 WT;TfR$^{mu/hu}$ and 4D9 APP^{SAA}; TfR$^{mu/hu}$ n = 4 mice/group).

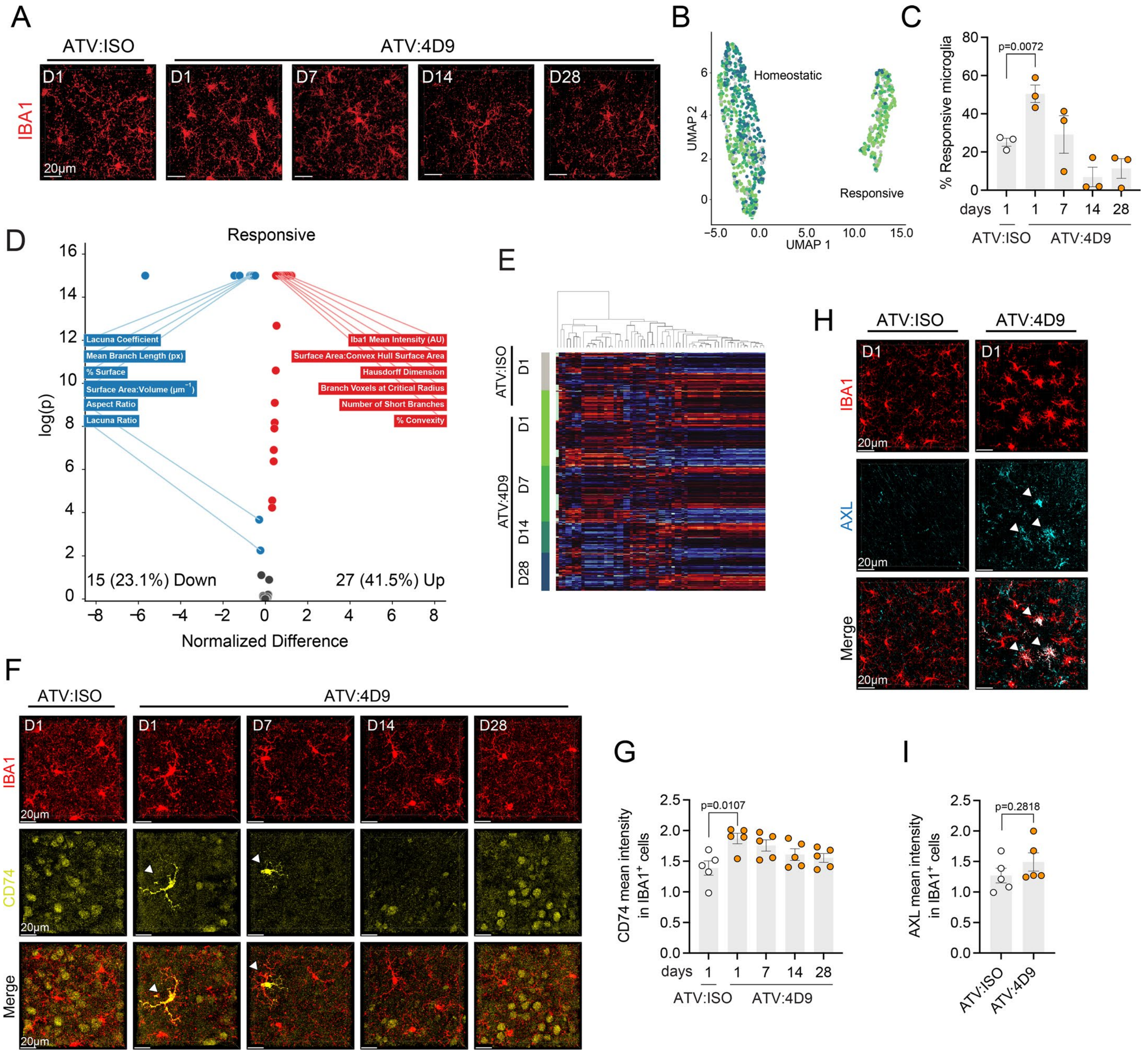

Extended Data Fig. 2 | ATV:4D9 induces temporally dynamic microglial morphology and marker expression. **(a)** Representative morphometric images of microglia in the cortex 1 day post dose with ATV:ISO or ATV:4D9 (10 mg kg^{-1}) at day 1-, 7-, 14-, and 28-days post dose. **(b)** UMAP plot of all microglia over time. **(c)** Percentage of microglia in the responsive cluster as a proportion of all segmented microglia over time (n = 3 male mice per group, two-tailed unpaired t-test between ATV:ISO and ATV:4D9 at day 1, mean ± SEM). **(d)** Volcano plot showing the top 6 differentially high and low normalized features comparing the responsive cluster to the homeostatic cluster. **(e)** Heatmap of normalized features for all segmented microglia (1,143 total cells) over time, measured across 65 morphometric and immunohistochemical features, grouped by treatment (rows) with features hierarchically clustered (columns). **(f)** Representative images of cortical brain sections co-stained with Iba1 and CD74 at 1-, 7-, 14-, 28-days days post 10 mg kg^{-1} dose of ATV:ISO or ATV:4D9. CD74$^+$ microglia are noted with white arrows. **(g)** Mean intensity of CD74 staining within segmented IBA1$^+$ microglia normalized to background CD74 intensity at each timepoint (n = 5 mice/group, two-tailed unpaired t-test between ATV:ISO and ATV:4D9 at day 1, mean ± SEM). **(h)** Representative images of cortical brain sections stained for IBA1 and AXL 1 day post dose of ATV:ISO or ATV:4D9. Double positive microglia are noted with white arrows. **(i)** Quantification of mean intensity of AXL staining within segmented IBA1$^+$ microglia normalized to background (n = 5 mice/group, two-tailed unpaired t-test, mean ± SEM).

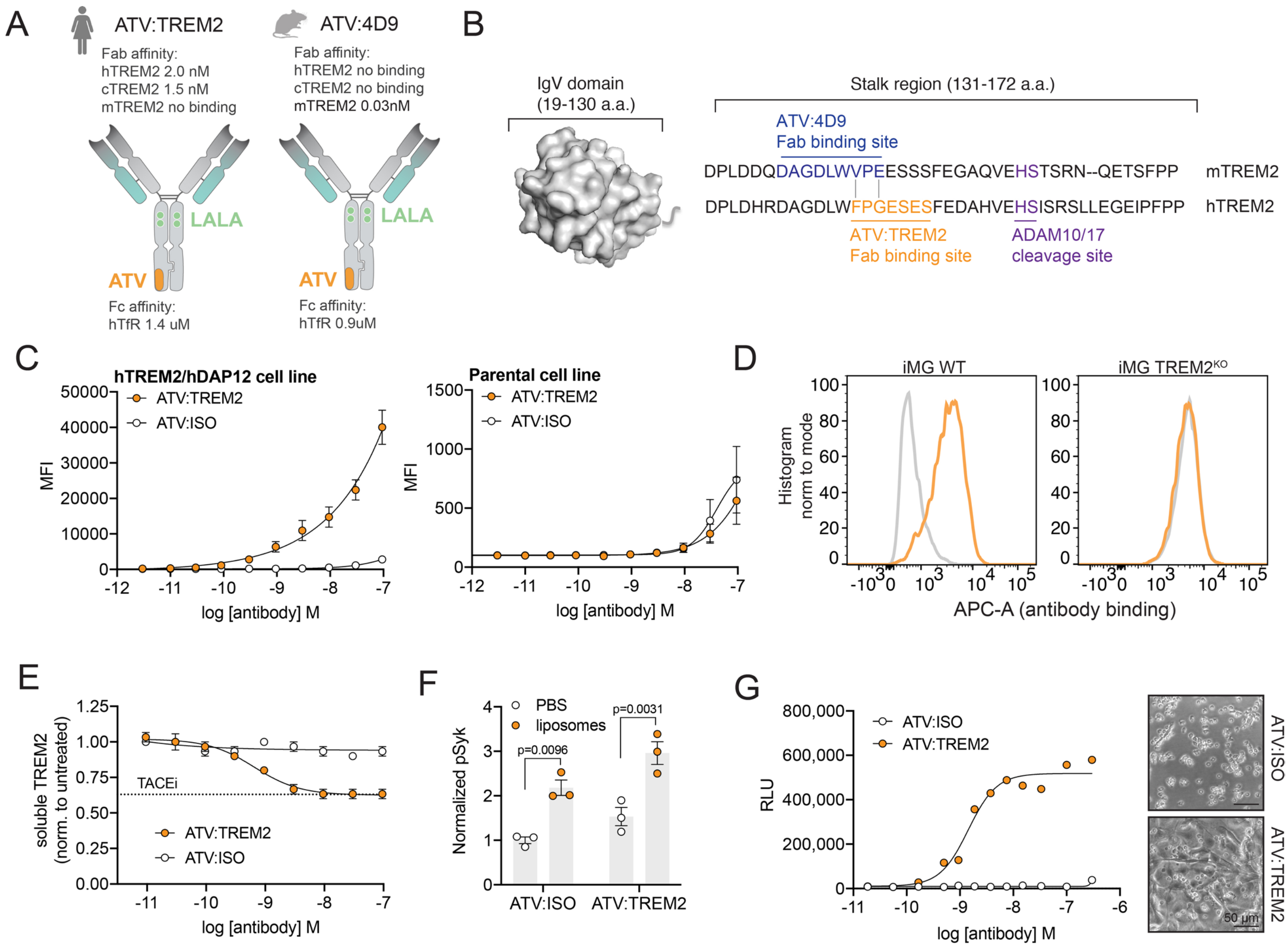

Extended Data Fig. 3 | ATV:4D9 and ATV:TREM2 demonstrate similar mechanisms of action with high affinity stalk binding epitopes and cellular function. **(a)** Antibody schematic comparing human specific ATV:TREM2 and mouse specific ATV:4D9 with high affinity TREM2 binding. **(b)** Epitope map of overlapping stalk binding regions for ATV:TREM2 and ATV:4D9 Fabs (space filled model of TREM2 ECD[1]). The binding epitope of ATV:4D9 antibody is located 12-amino acids N-terminal of the ADAM cleavage site at His157. **(c)** FACS analysis of cell binding of ATV:TREM2 to hTREM2-DAP12 HEK293 or parental cells. Endogenous TfR expression on HEK293 cells drives weak binding observed for ATV:ISO and ATV:TREM2 (n = 3 independent experiment, mean ± SEM). **(d)** FACS detection of ATV:TREM2 (100 nM) binding to WT and TREM2 KO iMG with isotype control (ATV:ISO). **(e)** Soluble TREM2 measured in the supernatant of hTREM2-DAP12 HEK293 cells dosed with ATV:TREM2 for 24 h shows dose-dependent reduction of sTREM2 to levels similar to 1 uM GM6001 (n = 3 independent experiment, mean ± SEM). **(f)** ATV:TREM2 and lipid ligands induce pSyk signaling in iMG 24 h post antibody exposure (n = 3 independent experiments, Tukey's multiple comparisons test, mean ± SEM). **(g)** Human monocytes cultured in limited M-CSF with plate coated ATV:TREM2 or ATV:ISO shows dose-dependent activity of ATV:TREM2 (EC50 0.95 +/− 0.45 nM). Representative data from one out of four human donors are shown.

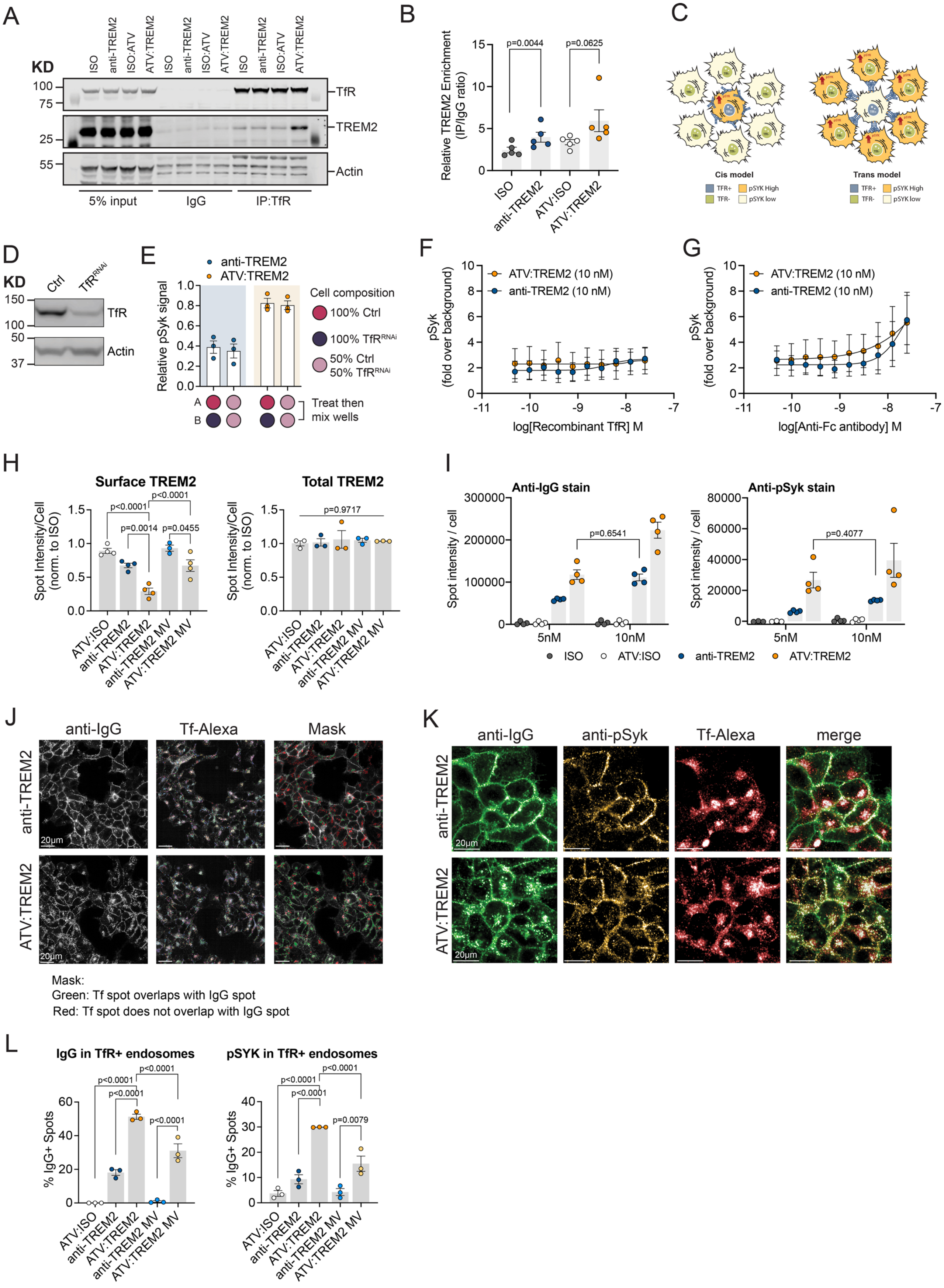

Extended Data Fig. 4 | See next page for caption.

https://doi.org/10.1038/s41593-022-01240-0

Extended Data Fig. 4 | ATV promotes TfR-TREM2 receptor complex formation and internalization and endosomal TREM2 signaling. (**a**) Representative Western blot of co-IP of TREM2 with TfR. hTREM2-DAP12 HEK293 cells were treated with 100 nM ATV:TREM2, anti-TREM2, or isotype controls for 5 min at 37 °C. (**b**) Co-IP quantification of Western blot from (A) (n = 6 independent experiments; two-tailed paired t-test for ISO vs anti-TREM2; two tailed Wilcoxon test ATV:ISO vs ATV:TREM2, mean ± SEM). (**c**) Schematic illustration of *cis*- and *trans*-activation models that could mediate pSyk enhancement by ATV:TREM2. (**d**) Western blot validation of TfR knockdown in the TfR^{RNAi} cell line. (**e**) Cell based cis/trans assay indicates ATV:TREM2 enhances pSyk activity in cis. Relative pSYK signal is expressed as raw pSYK AlphaLisa value normalized to ATV:TREM2 treated control (n = 3 independent experiment, mean ± SEM). **(f)** Normalized pSyk signal measured by AlphaLisa assay. TfR^{RNAi} cells were treated with 10 nM anti-TREM2 or ATV:TREM2 pre-incubated with a dose titration of recombinant TfR protein for 5 min at 37 °C (n = 3 independent experiment, mean ± SEM). (**g**) Normalized pSyk signal detected by AlphaLisa. TfR^{RNAi} cells were treated with 10 nM anti-TREM2 or ATV:TREM2 pre-incubated with a dose titration of a secondary anti-human IgG Fc antibody for 5 min at 37 °C (n = 3 independent experiment, mean ± SEM) **(h)** Immunofluorescence microscopy of hTREM2-DAP12 HEK293 cells demonstrates reduction of surface TREM2 levels with ATV:TREM2 vs anti-TREM2, no changes in total TREM2 levels, consistent with re-distribution of the receptor from the plasma membrane to endosomes (n = 4 independent experiments except for anti-TREM2 MV (n = 3), Tukey's multiple comparisons test, mean ± SEM). **(i)** hTREM2-DAP12 HEK293 cells dosed with antibody for 10 minutes shows that at similar amounts of bound antibody detected by anti-IgG (representing 5 nM of ATV:TREM2 and 10 nM of anti-TREM2, n = 4 independent experiments, Tukey's multiple comparisons test, mean ± SEM**(j)** Images depicting masking algorithm used to identify whether TfR-Alexa-647 labeled recycling endosomes (rainbow spots in middle images) either contain (green spots in right-most images) or do not contain (red spots in right-most images) IgG spots (white spots in left-most image) upon dosing with anti-TREM2 (top row) or ATV:TREM2 (bottom row) for 10 minutes with 10 nM antibody. **(k)** Representative images for hTREM2-DAP HEK293 cells dosed with 10 nM antibody for 10 minutes including 20 ug mL^{-1} TfR-Alexa-647, fixed, permeabilized, and stained with anti-IgG and anti-pSyk. IF shows ATV increased colocalization of antibody with pSyk in early endosomes. **(l)** Quantification of percent of IgG or pSyk spots localized within Tf-positive endosomes (n = 3 independent experiments, Tukey's multiple comparisons test, mean ± SEM).

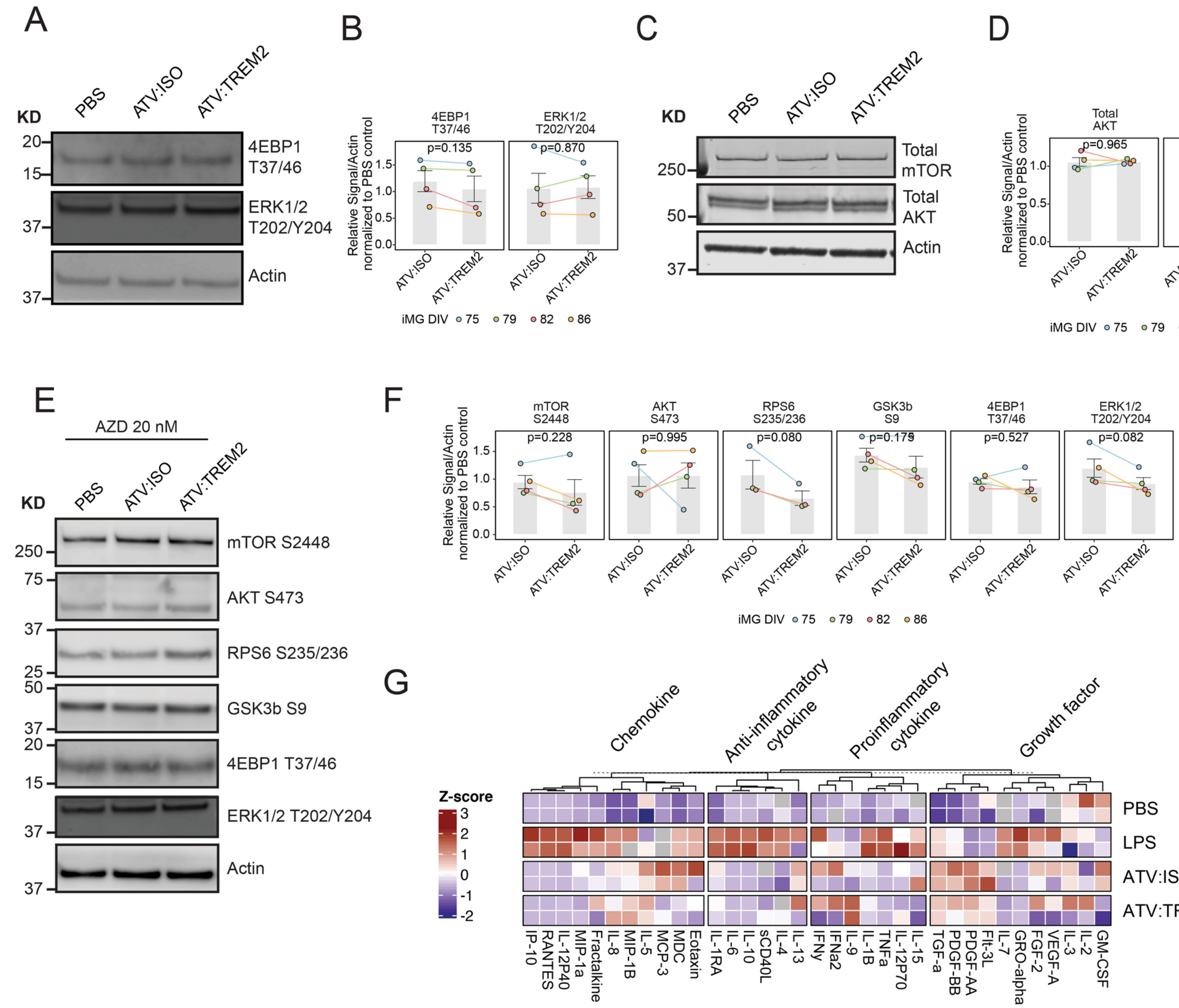

Extended Data Fig. 5 | ATV:TREM2 does not promote ERK1/2 phosphorylation or a proinflammatory signature in microglia. (**a**) Representative Western blot images of phosphorylation of 4EBP1 (T37/46) and ERK1/2 (T202/Y204) in WT iMGs treated for 96 h with 100 nM ATV:TREM2 or an isotype control. (**b**) Quantification of p4EBP1 (T37/46) and pERK1/2 (T202/Y204) normalized to actin. Relative expression was calculated by normalizing to PBS vehicle control for each experiment (n = 4 independent experiments, two-tailed paired t-test, mean ± SEM). (**c**) Representative Western blot images of total protein levels of mTOR and AKT in WT iMG treated for 96 h with 100 nM ATV:TREM2 or an isotype control. (**d**) Quantification of total mTOR and AKT protein normalized to actin. Relative expression was calculated by normalizing to PBS control for each experiment (n = 4 independent experiments, two-tailed paired t-test, mean ± SEM). **e**) Representative Western blot images for p-mTOR (S2448), pAKT (S473), pGSK3b (S9) pRPS6 (S235/236), p4EBP1 (T37/46) and pERK1/2 (T202/Y204) showing inhibition of mTOR pathway activation in WT iMG co-treated with 20 nM AZD8055 and 100 nM ATV:TREM2 after 96 h. (**f**) Quantification of phosphorylation targets shown in (E). Phosphorylation signals were normalized to actin. Relative expression was calculated by normalizing to PBS vehicle control for each experiment (n = 4 independent experiments, two-tailed paired t-test, mean ± SEM)). (**g**) Heatmap of human cytokine profiling in supernatant from WT iMG treated with 100 nM ATV:TREM2 for 96 h. Media collected from iMG treated with 10 ng mL^{-1} LPS for 24 h was used for comparison.

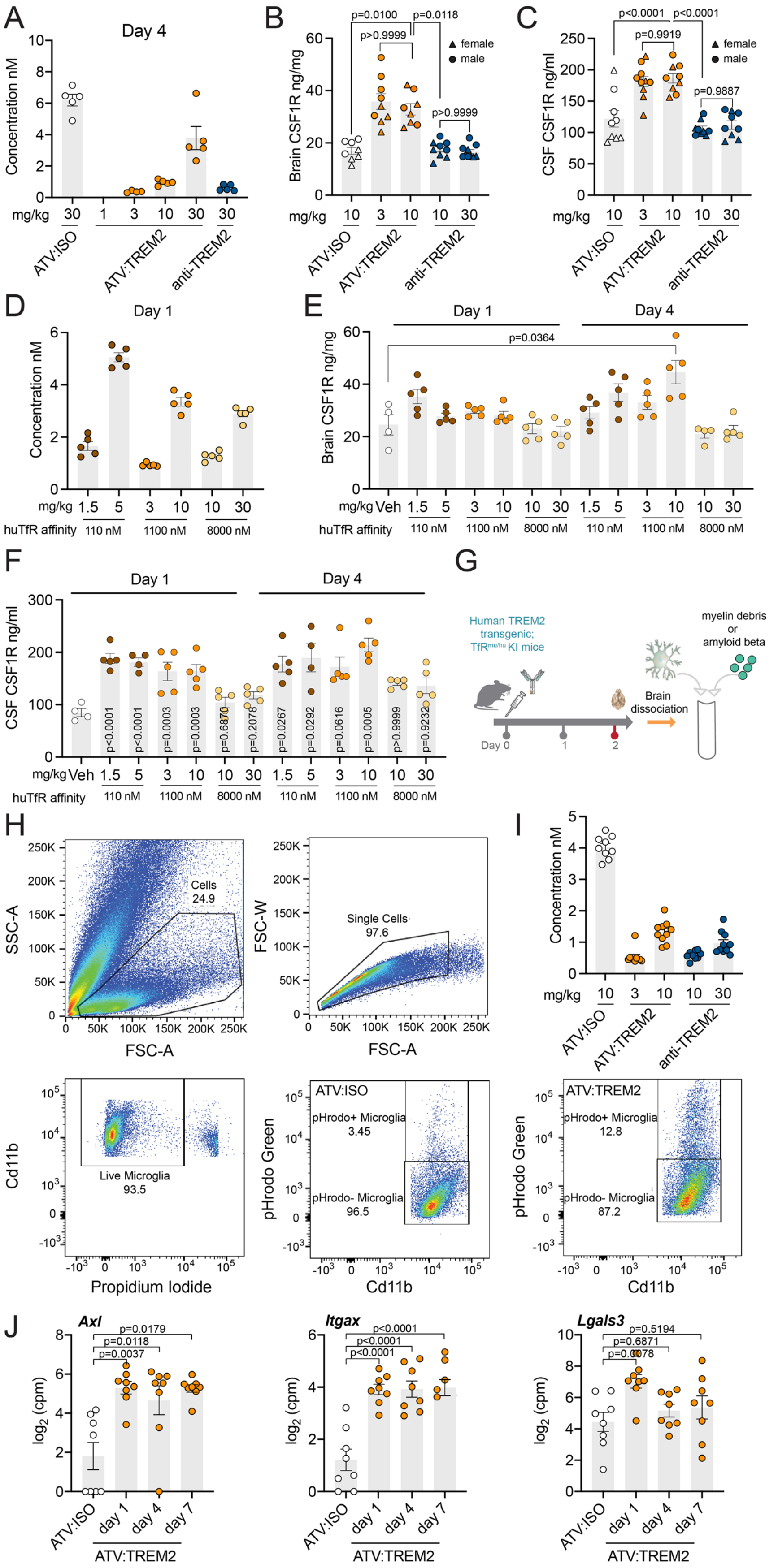

Extended Data Fig. 6 | See next page for caption.

Extended Data Fig. 6 | ATV:TREM2 increases phagocytosis and CSF1R in human TREM2 tg;TfR$^{mu/hu}$ mice. (a) Antibody levels detected in brain lysates by ELISA shows increased brain exposure of ATV:TREM2 (30 mg kg^{-1}) compared anti-TREM2 (30 mg kg^{-1}) and comparable brain exposure for ATV:TREM2 at 10 mg kg^{-1} and anti-TREM2 at 30 mg kg^{-1} at day 4 post-dose. (n = 5 mice/group except for ATV:TREM2 3 mg kg^{-1} (n = 4)). **(b)** ATV:TREM2 increases CSF1R in the brain compared to brain exposure matched anti-TREM2 day 2 post dose (n = [8, 9, 8, 9, 10]mice/group, Kruskal-Wallis test, mean ± SEM). (**c**) CSF1R analysis in CSF same as in B. (n = [8, 9, 8, 9, 10]mice/group, Tukey's multiple comparisons test, mean ± SEM) (**b**-**c**) Circles represents male mice and triangle represents female mice. **(d)** Detection of antibody concentrations show matched brain exposure of three ATV:TREM2 molecules with different ATV affinities 1-day post-dose (n = 5 mice/group). **(e-f)** High and mid-affinity ATV:TREM2 molecules induce comparable increase of CSF1R in the brain (**e**) n = 5 mice/group except for Vehicle (Veh) and day 4 10 mg kg^{-1} 8,000 nM (n = 4, Kruskal-Wallis test, compared to vehicle group) and CSF **(f)** (n = 5 mice/group, except for Veh and day 4 5 mg kg^{-1} 110 nM n = 4), Dunnett's multiple comparisons test for day 1, Kruskal-Wallis test for day 4) day 1 and 4 post dose whereas low-affinity ATV:TREM2 induces a weak elevation of CSF1R in CSF at day 4 (n = 4-5 mice/group, mean ± SEM). **(g)** Schematic of experimental approach to evaluate in vivo dosed antibody impact to microglial phagocytosis ex vivo. A single dose of ATV:TREM2, anti-TREM2, or ATV:ISO was administrated to human TREM2 tg; TfR$^{mu/hu}$ KI mice and brain microglia were isolated 2 days post dose for ex vivo myelin phagocytosis analysis. The same method was used to assess amyloid phagocytosis. **(h)** FACS gating strategy to quantify pHrodo-myelin positive microglia. After treatment with pHrodo-green myelin and staining, cell suspensions containing microglia were analyzed using BD FACS Aria III. Single cells were separated from debris by FSC and SSC characteristics. Live microglia were identified as a population of CD11b^{+} and propidium iodide^{negative} cells. pHrodo-myelin uptake was then quantified in 20,000 microglia recorded from each sample. **(i)** Antibody concentrations were detected in brain lysates by ELISA which shows comparable levels of ATV:TREM2 and anti-TREM2 day 2 post dose (n = [9, 10, 10, 9, 10] mice/group). **(j)** ATV:TREM2 induces transcription of genes associated with phagocytosis. *Axl, Itgax, Lgals3* mRNA levels were detected in isolated brain microglia after peripheral administration of 10 mg kg^{-1} ATV:TREM2 1-, 4-, and 7-days post dose. Graphs represent bulk mRNA measured by RNA-seq. Data shown as $\log_2$ counts per million (with a pseudocount of 1 added) in each biological replicate (n = 8 mice/group, each group compared to ATV:ISO group, Kruskal-Wallis test for Axl, Dunnett's multiple comparisons for *Itgax* and *Lgals3*, mean ± SEM).

https://doi.org/10.1038/s41593-022-01240-0

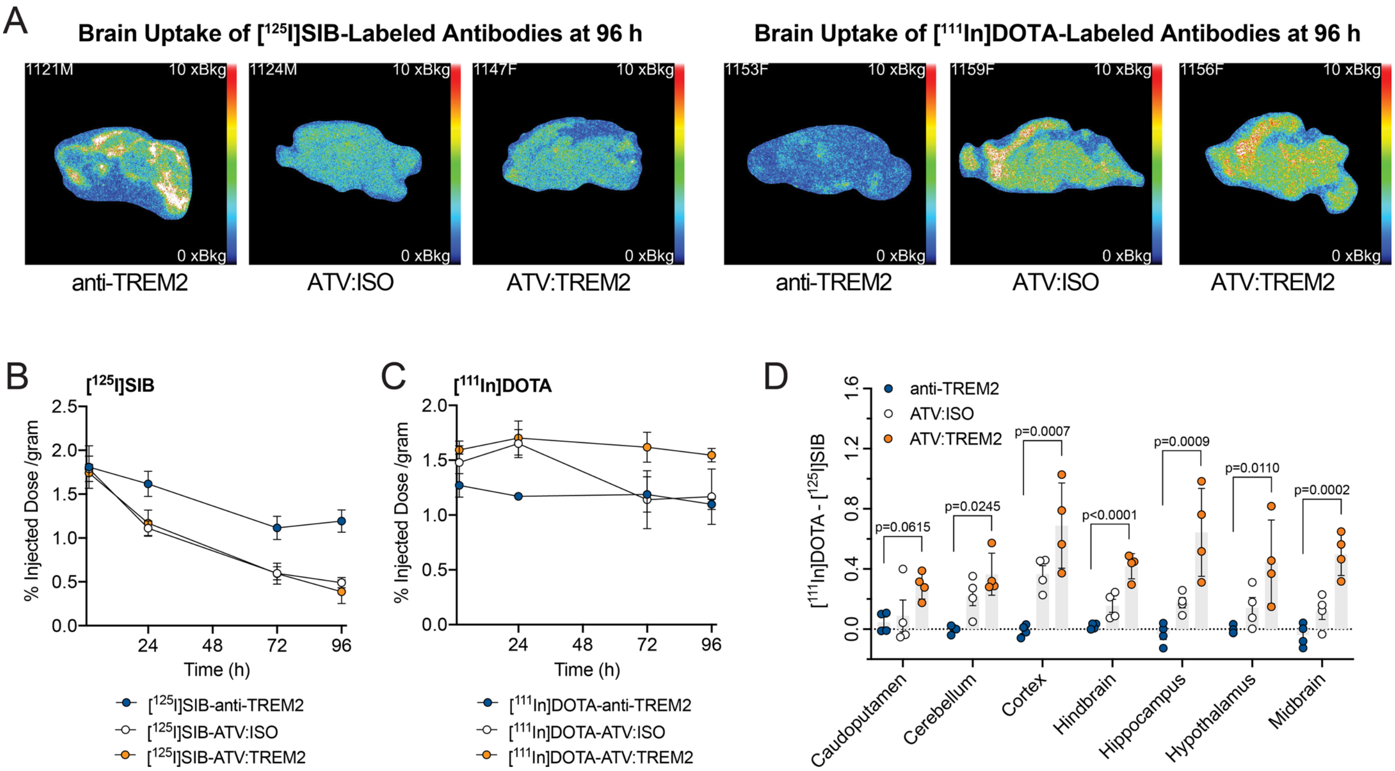

Extended Data Fig. 7 | Single photon emission computed tomography imaging demonstrates increased ATV:TREM2 biodistribution and catabolism in brain. (a) Representative autoradiography images of sagittal brain sections from WT; hTREM2 tg; TfR$^{mu/hu}$ mice 96 h after administration of ATV:TREM2, anti-TREM2, and ATV:ISO radiolabeled with [^{111}In]DOTA or [^{125}I]SIB. **(b,c)** Longitudinal SPECT/CT imaging quantification of whole-brain uptake of single dose (100 µCi, 200 µL, 1.5 mg kg^{-1}, IV) ATV:TREM2, anti-TREM2, and ATV:ISO, radiolabeled with [^{125}I]SIB **(b)** or [^{111}In]DOTA **(c)** in WT; hTREM2 tg; TfR$^{mu/hu}$ mice. Whole brain %ID/g was corrected for contribution from cerebral blood volume. Data are represented as mean +/− SEM (n = 3 mice/group). **(d)** Percent of catabolized ATV:TREM2 in several brain regions 96 h after single dose exceeds that of ATV:ISO control. [^{111}In]DOTA and [^{125}I]SIB signal was quantified by *ex vivo* gamma counting in resected brain regions, and percent of catabolized antibody was estimated by subtracting %ID/g for [^{125}I]SIB signal from that of [^{111}In]DOTA signal (n = 4 mice/group, one-way ANOVA with Dunnett's multiple comparison test for each region, except for cerebellum which applied Brown-Forsythe and Welch ANOVA tests, mean ± SEM).

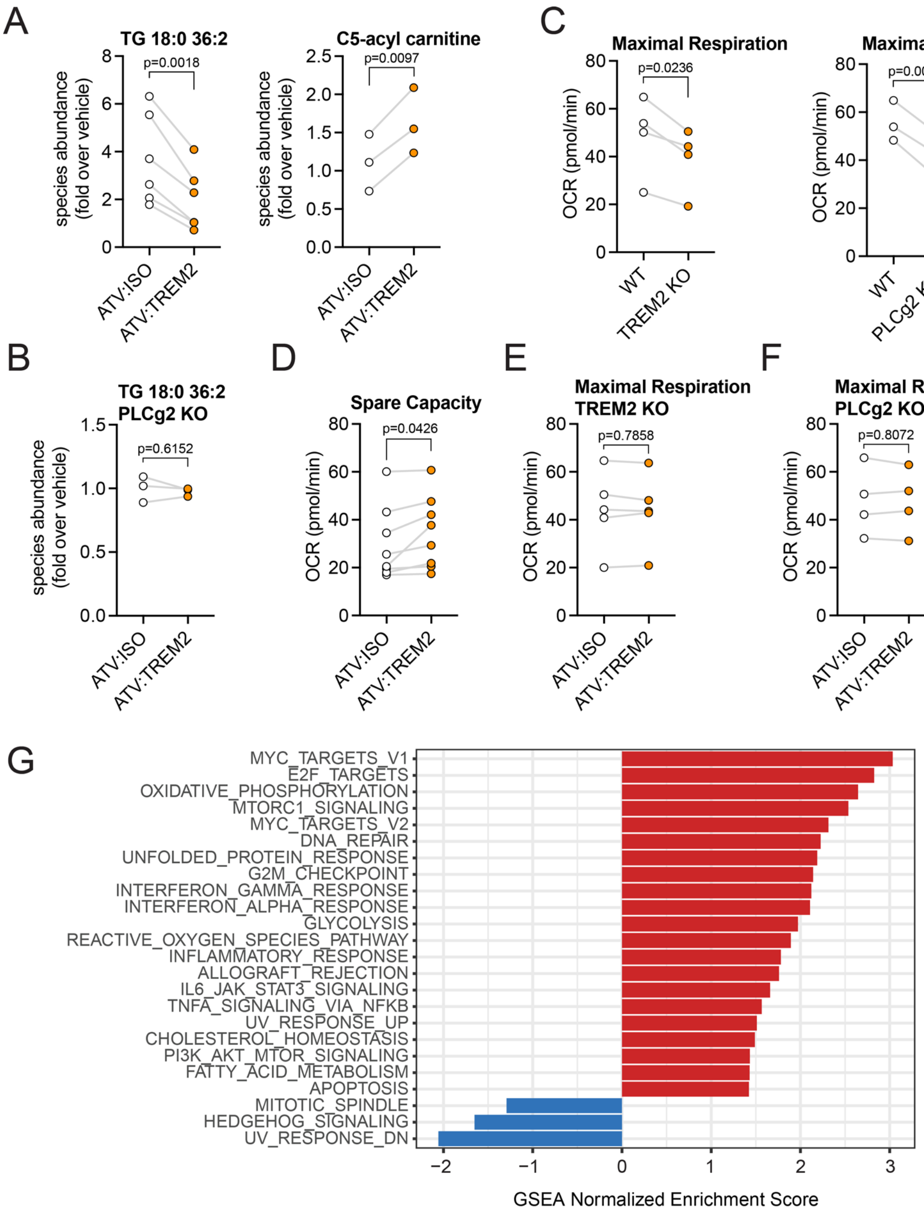

Extended Data Fig. 8 | ATV:TREM2 increases microglial metabolism in a *TREM2* and *PLCG2*-dependent manner. **(a)** Additional species of triglycerides (TG) and short chain carnitines modulated in iMG with ATV:TREM2 treatment (n = 3-5 independent experiment, two-tailed paired t-test, mean ± SEM). **(b)** ATV:TREM2 does not modulate TG in *PLCG2* KO iMG (n = 3 independent experiment, two-tailed paired t-test, mean ± SEM). **(c)** Maximal respiration measured by Seahorse fatty acid oxidation kit is reduced in both *TREM2* KO and *PLCG2* KO iMG (n = 3-4 independent experiment, two-tailed paired t-test, mean ± SEM). **(d)** ATV:TREM2 increased spare capacity measured by Seahorse fatty acid oxidation kit (n = 8 independent experiment, two-tailed paired t-test, mean ± SEM). **(e)** ATV:TREM2 does not modulate maximal respiration or spare capacity in *TREM2* KO iMG (n = 4 independent experiment, two-tailed paired t-test, mean ± SEM). **(f)** ATV:TREM2 does not modulate maximal respiration and spare capacity *PLCG2* KO iMG (n = 4 independent experiment, two-tailed paired t-test, mean ± SEM). **(g)** RNAseq analysis of brain microglia isolated from hTREM2 tg; TfR$^{mu/hu}$ mice dosed with 10 mg kg^{-1} ATV:TREM2. GSEA for top pathways based on a p-value cutoff of 0.05 for up- or downregulated gene sets 1 day post ATV:TREM2 dose.

nature portfolio

Corresponding author(s): Kathryn M. Monroe, Pascal E. Sanchez

Last updated by author(s): Sep 8, 2022

Reporting Summary

Nature Portfolio wishes to improve the reproducibility of the work that we publish. This form provides structure for consistency and transparency in reporting. For further information on Nature Portfolio policies, see our Editorial Policies and the Editorial Policy Checklist.

Statistics

For all statistical analyses, confirm that the following items are present in the figure legend, table legend, main text, or Methods section.

n/a	Confirmed	
☐	☒	The exact sample size (*n*) for each experimental group/condition, given as a discrete number and unit of measurement
☐	☒	A statement on whether measurements were taken from distinct samples or whether the same sample was measured repeatedly
☐	☒	The statistical test(s) used AND whether they are one- or two-sided *Only common tests should be described solely by name; describe more complex techniques in the Methods section.*
☒	☐	A description of all covariates tested
☐	☒	A description of any assumptions or corrections, such as tests of normality and adjustment for multiple comparisons
☐	☒	A full description of the statistical parameters including central tendency (e.g. means) or other basic estimates (e.g. regression coefficient) AND variation (e.g. standard deviation) or associated estimates of uncertainty (e.g. confidence intervals)
☐	☒	For null hypothesis testing, the test statistic (e.g. *F*, *t*, *r*) with confidence intervals, effect sizes, degrees of freedom and *P* value noted *Give P values as exact values whenever suitable.*
☒	☐	For Bayesian analysis, information on the choice of priors and Markov chain Monte Carlo settings
☒	☐	For hierarchical and complex designs, identification of the appropriate level for tests and full reporting of outcomes
☒	☐	Estimates of effect sizes (e.g. Cohen's *d*, Pearson's *r*), indicating how they were calculated

Our web collection on statistics for biologists contains articles on many of the points above.

Software and code

Policy information about availability of computer code

Data collection	ImageStudioLite software (Li-COR, Version 5.2.5), EnVision Workstation software (Perkin Elmer, Version #1.14.3049.528), Opera Phenix High Content Imager Harmony software (Perkin Elmer, Version v5.1.2167.302), MSD software (Methodical Mind, V1.0.38),Zeiss Axioscan.Z1 slide scanner (ZEN blue v3.5.093.00005, Carl Zeiss Microscopy), spinning disc confocal microscope (Zeiss AxioObserver Z1, Carl Zeiss Microscopy, ZEN blue v2.6.18299.3), canning confocal microscope (Leica SP8; Leica Microsystems, Inc, Leica Application Suite X v3.5.7.23225), flow cytometer Canto/Aria III (BD FACSDiva software V9.0), Tera-Tomo 3D (Mediso Ltd, Hungary).
Data analysis	Prism Version 9.3.1 (350), R Studio (Version 1.4.1717), Python (Version 3.10.8), STAR v2.7.1a, scRNAseq Seraut (Version 4),Bulk RNAseq RNAseq: Bioconductor (version 3.13),Cell Ranger (v7.0.0 for WT study; v6.1.1 for AD study), Imaris (Bitplane, V9.9.1), PMOD (V3.5, PMOD technologies, Switzerland). All of the code used to process and analyze these data are made available via GitHub: https://github.com/denalitherapeutics/Lengerich_natneuro_2022. R packages used are listed via Github here: https://github.com/denalitherapeutics/Lengerich_natneuro_2022/blob/main/renv.lock.

For manuscripts utilizing custom algorithms or software that are central to the research but not yet described in published literature, software must be made available to editors and reviewers. We strongly encourage code deposition in a community repository (e.g. GitHub). See the Nature Portfolio guidelines for submitting code & software for further information.

Data

Policy information about availability of data

All manuscripts must include a data availability statement. This statement should provide the following information, where applicable:

- Accession codes, unique identifiers, or web links for publicly available datasets
- A description of any restrictions on data availability
- For clinical datasets or third party data, please ensure that the statement adheres to our policy

Raw and processed single-cell/bulk RNA-seq data have been deposited at the NCBI GEO repository under accession numbers: GSE198987, GSE199154, GSE200275, and GSE209912. The metabolomics data have been uploaded to the MetaboLights repository with study ID MTBLS6543.

Field-specific reporting

Please select the one below that is the best fit for your research. If you are not sure, read the appropriate sections before making your selection.

☒ Life sciences ☐ Behavioural & social sciences ☐ Ecological, evolutionary & environmental sciences

For a reference copy of the document with all sections, see nature.com/documents/nr-reporting-summary-flat.pdf

Life sciences study design

All studies must disclose on these points even when the disclosure is negative.

Sample size	No statistical methods were used to predetermine sample size. Sample sizes were chosen as standard in the field (Schlepckow et al., EMBO 2020). For in vivo study, sample size "n" represents the number of animals used. For in vitro study, sample size "n" represents the number of independent experiments performed.
Data exclusions	No data were excluded from the study.
Replication	The exact number of repetitions (individual data points from each cells and/or animal) are indicated in figures or figure legends. For in vitro experiments, at least 3 independent experiments were performed as biological replication. All replication were successful.
Randomization	For in vivo experiments, animals/samples were randomized before drug treatment to cover sex/genotype/drugs/etc for balancing potential batch effects. No randomization was performed for in vitro studies.
Blinding	The samples were not blinded during initial study planning to ensure that the number of groups of mice were randomized and balanced, while age and sex matched. RNAseq datasets were not blinded for analysis. Image analysis and ex-vivo assays were performed in a blinded fashion. In vitro studies were performed unblinded. The PET imaging analysis was not blinded, however we used an automated pipeline72,73 such that the operator cannot influence/bias the results since the coregistration and the voi extraction is a defined procedure.

Reporting for specific materials, systems and methods

We require information from authors about some types of materials, experimental systems and methods used in many studies. Here, indicate whether each material, system or method listed is relevant to your study. If you are not sure if a list item applies to your research, read the appropriate section before selecting a response.

Materials & experimental systems

n/a	Involved in the study	
☐	☒	Antibodies
☐	☒	Eukaryotic cell lines
☒	☐	Palaeontology and archaeology
☐	☒	Animals and other organisms
☒	☐	Human research participants
☒	☐	Clinical data
☒	☐	Dual use research of concern

Methods

n/a	Involved in the study	
☒	☐	ChIP-seq
☐	☒	Flow cytometry
☒	☐	MRI-based neuroimaging

Antibodies

Antibodies used	ATV:TREM2, anti-TREM2, monovalent versions thereof, ATV:4D9, anti-4D9, and isotype controls were produced at Denali according to Materials and Methods. Commercial Antibody used are listed below: Name Application Dilution Source Cat# Clone mTOR (7C10) WB 1/500 CST 2983T 7C10 Phospho-mTOR (Ser2448) WB 1/500 CST 5536T D9C2 Phospho-Akt (Ser473) WB 1/250 CST 9271T Polyclonal

AKT WB 1/500 CST 4691T C67E7
Phospho-RPS6 (Ser235/236) WB 1/500 CST 4858T D57.2.2E
Phospho-GSK-3β (Ser9) WB 1/500 CST 5558T D85E12
β-Actin WB 1/1000 CST 58169S E4D9Z
Phospho-4E-BP1 (Thr37/46) WB 1/500 CST 2855T 236B4
Phospho-Erk1/2 (Thr202/Tyr204) WB 1/1000 CST 4370S D13.14.4E
TREM2 WB, IP, ICC 1/500 R and D systems AF1828 Polyclonal
CD31 WB 1/500 CST 77699 D8V9E
GAPDH WB 1/500 Abcam Ab181603 EPR16884
CLDN5 WB 1/500 Invitrogen 35-2500 4C3C2
normal goat IgG (R&D, AB-108-C) IP IgG control 2 ug per 400-500 ug lysate R and D systems AB-108-C Polyclonal
TfR_DNLI_#1 IP NA Denali Therapeutics NA DC0002
TfR_DNLI_#2 TfR blocking NA Denali Therapeutics NA DC0637
TfR ICC, WB 1/250 Thermofisher 13-6800 H68.4
EEA1 ICC 1/250 BD Biosciences 610457 14
phospho-Syk (Tyr525/526) ICC 1/250 CST 2710 C87C1
CD11b-BV421 FACS 1/100 BioLegend 101251, 101235 M1/70
CD45-APC FACS 1/100 BD Biosciences 559864 30-F11
anti-mouse CD16/32 FACS 1/20 BioLegend 101320 93
Axl IHC 1/25 R and D systems AF854 Polyclonal
Iba1_guinea pig IHC 1/500 Synaptic Systems HS-234 308 Gp311H9
Iba1_goat IHC 1/500 Novus NB100-1028 Polyclonal
Iba1_rabbit IHC 1/500 abcam ab178847 monoclonal
CD74 IHC 1/500 abcam ab245692 In-1
donkey anti-human IgG ELISA 1 ug/mL Jackson Immunoresearch 709-006-098 Polyclonal
HRP conjugated goat anti-human IgG ELISA 0.02 ug/mL Jackson Immunoresearch 109-036-098 Polyclonal
biotinylated anti-human TREM2 polyclonal antibody MSD 1 ug/mL R and D systems BAF1828 Polyclonal
biotinylated anti-mouse TREM2 polyclonal antibody (R&D Systems BAF1828 for human, BAF1729 for mouse MSD 1 ug/mL R and D systems BAF1729 Polyclonal
anti-mouse transferrin receptor antibody kit MSD capture.ab=0.125 ug/mL; detector.ab= 0.25 ug/mL Abcam ab256631 monoclonal

Validation

All Denali antibodies were characterized as described in the manuscript for specificity and binding by biacore and FACS-based cell binding using KO cell lines and overexpression cell lines (See Extended data figure 3, Table 1).
Commercial antibodies were validated by suppliers as shown below: Antibody Validation_link
mTOR (7C10) https://www.cellsignal.com/products/primary-antibodies/mtor-7c10-rabbit-mab/2983
Phospho-mTOR (Ser2448) https://www.cellsignal.com/products/primary-antibodies/phospho-mtor-ser2448-d9c2-xp-rabbit-mab/5536?site-search-type=Products&N=4294956287&Ntt=5536t&fromPage=plp&_requestid=3313777
Phospho-Akt (Ser473) https://www.cellsignal.com/products/primary-antibodies/phospho-akt-ser473-antibody/9271?site-search-type=Products&N=4294956287&Ntt=9271t&fromPage=plp&_requestid=3313824
AKT https://www.cellsignal.com/products/primary-antibodies/akt-pan-c67e7-rabbit-mab/4691?site-search-type=Products&N=4294956287&Ntt=4691t&fromPage=plp&_requestid=3325825
Phospho-RPS6 (Ser235/236) https://www.cellsignal.com/products/primary-antibodies/phospho-s6-ribosomal-protein-ser235-236-d57-2-2e-xp-rabbit-mab/4858?site-search-type=Products&N=4294956287&Ntt=4858t&fromPage=plp&_requestid=3314019
Phospho-GSK-3β (Ser9) https://www.cellsignal.com/products/primary-antibodies/phospho-gsk-3b-ser9-d85e12-xp-rabbit-mab/5558?site-search-type=Products&N=4294956287&Ntt=5558t&fromPage=plp&_requestid=3314040
β-Actin https://www.cellsignal.com/products/primary-antibodies/b-actin-e4d9z-mouse-mab/58169?site-search-type=Products&N=4294956287&Ntt=58169s&fromPage=plp&_requestid=3314118
Phospho-4E-BP1 (Thr37/46) https://www.cellsignal.com/products/primary-antibodies/phospho-4e-bp1-thr37-46-236b4-rabbit-mab/2855?site-search-type=Products&N=4294956287&Ntt=2855t&fromPage=plp&_requestid=3314156
Phospho-Erk1/2 (Thr202/Tyr204) https://www.cellsignal.com/products/primary-antibodies/phospho-p44-42-mapk-erk1-2-thr202-tyr204-d13-14-4e-xp-rabbit-mab/4370?site-search-type=Products&N=4294956287&Ntt=4370s&fromPage=plp&_requestid=3318000
TREM2 https://www.rndsystems.com/products/human-trem2-antibody_af1828
CD31 https://www.cellsignal.com/products/primary-antibodies/cd31-pecam-1-d8v9e-xp-rabbit-mab/77699
GAPDH https://www.abcam.com/gapdh-antibody-epr16884-loading-control-ab181603.html
CLDN5 https://www.thermofisher.com/antibody/product/Claudin-5-Antibody-clone-4C3C2-Monoclonal/35-2500
normal goat IgG (R&D, AB-108-C) https://www.rndsystems.com/products/normal-goat-igg-control_ab-108-c
TfR_DNLI_#1 https://www.science.org/doi/10.1126/scitranslmed.aay1359?url_ver=Z39.88-2003&rfr_id=ori:rid:crossref.org&rfr_dat=cr_pub%20%200pubmed
TfR_DNLI_#2 https://www.science.org/doi/10.1126/scitranslmed.aay1359?url_ver=Z39.88-2003&rfr_id=ori:rid:crossref.org&rfr_dat=cr_pub%20%200pubmed
TfR https://www.thermofisher.com/antibody/product/Transferrin-Receptor-Antibody-clone-H68-4-Monoclonal/13-6800
EEA1 https://www.bdbiosciences.com/en-us/products/reagents/microscopy-imaging-reagents/immunofluorescence-reagents/purified-mouse-anti-eea1.610457
phospho-Syk (Tyr525/526) https://www.cellsignal.com/products/primary-antibodies/phospho-syk-tyr525-526-c87c1-rabbit-mab/2710
CD11b-BV421 https://www.citeab.com/antibodies/2082933-101251-brilliant-violet-421-anti-mouse-human-cd11b
CD45-APC https://www.bdbiosciences.com/en-us/products/reagents/flow-cytometry-reagents/research-reagents/single-color-antibodies-ruo/apc-rat-anti-mouse-cd45.559864
anti-mouse CD16/32 https://www.biolegend.com/en-us/punchout/search-results/trustain-fcx-anti-mouse-cd16-32-antibody-5683?GroupID=BLG9237
Axl https://www.rndsystems.com/products/mouse-axl-antibody_af854?gclid=Cj0KCQiA4OybBhCzARIsAIcfn9nmYA1ndIVozmw91Qy2ga_a4D_VN3XomInOEd8lq8SERFV0Y7Ou2PsaAl4eEALw_wcB&gclsrc=aw.ds
Iba1_guinea pig https://www.sysy.com/product/HS-234308
Iba1_goat https://www.novusbio.com/products/aif-1-iba1-antibody_nb100-1028
Iba1_rabbit https://www.abcam.com/iba1-antibody-epr16589-ab178847.html

CD74 https://www.abcam.com/cd74-antibody-in-1-ab245692.html
donkey anti-human IgG https://www.jacksonimmuno.com/catalog/products/709-006-098
HRP conjugated goat anti-human IgG https://www.jacksonimmuno.com/catalog/products/109-036-098
biotinylated anti-human TREM2 polyclonal antibody https://www.rndsystems.com/products/human-trem2-biotinylated-antibody_baf1828
biotinylated anti-mouse TREM2 polyclonal antibody (R&D Systems BAF1828 for human, BAF1729 for mouse https://www.rndsystems.com/products/mouse-trem2-biotinylated-antibody_baf1729
anti-mouse transferrin receptor antibody kit https://www.abcam.com/mouse-transferrin-receptor-antibody-pair-bsa-and-azide-free-ab256631.html

Eukaryotic cell lines

Policy information about cell lines

Cell line source(s)	HEK293 (RRID:CVCL_0045); iPSC1 (RRID:CVCL_D086); Expi293F (RRID:CVCL_D615)
Authentication	Cell lines were not authenticated, but TREM2 expression was regularly validated.
Mycoplasma contamination	Confirmed negative for mycoplasma in house.
Commonly misidentified lines (See ICLAC register)	These cell lines were not listed in the commonly misidentified lines from ICLAC registry.

Animals and other organisms

Policy information about studies involving animals; ARRIVE guidelines recommended for reporting animal research

Laboratory animals	The genotype, age and sex information of mouse models used in this study are summarized in Supplementary Table 2. Mice are maintained on C57BL/6J genetic background. Mouse husbandry and experimental procedures were approved by Denali Institutional Animal Care and Use Committee. All animal experiments at DZNE were performed in accordance with animal-handling laws of the state of Bavaria (Germany). Housing conditions included standard pellet food and water provided ad libitum, a 12-h light–dark cycle at temperature of 22°C with maximal 5 mice per cage and cage replacement once per week with regular health monitoring. Animals used in this study: WT; TfRmu/hu mice, mixed sex, from 2 to 8 months of age; WT;AppSAA; TfRmu/hu mice, male, 8 months; hTREM2 tg; TfRmu/hu mice, mixed sex, from 3 to 6 months of age; 5xFAD; hTREM2 tg; TfRmu/hu, mixed sex, 4.5 months. Female Lewis rats at 8 weeks of age were purchased from Charles River Laboratories (Strain Code 004) for antibody discovery for the TREM2 campaign.
Wild animals	No wild animals were used in the study.
Field-collected samples	No field collected samples were used in the study.
Ethics oversight	Denali Institutional Animal Care and Use Committee

Note that full information on the approval of the study protocol must also be provided in the manuscript.

Flow Cytometry

Plots

Confirm that:

☒ The axis labels state the marker and fluorochrome used (e.g. CD4-FITC).

☒ The axis scales are clearly visible. Include numbers along axes only for bottom left plot of group (a 'group' is an analysis of identical markers).

☒ All plots are contour plots with outliers or pseudocolor plots.

☒ A numerical value for number of cells or percentage (with statistics) is provided.

Methodology

Sample preparation	Ex vivo phagocytosis: Mice were taken down two days post antibody treatment and brain was dissected out after PBS perfusion for single cell dissociation by the Adult Brain Dissociation Kit (Miltenyi Biotec, 130-107-677), according to the manufacturer’s protocol. Microglia number was measured by FACS using CountBright Absolute Counting Beads (Invitrogen, C36950) and samples were diluted to 500 microglia/ul in DPBS+0.5%BSA. 100ul of the resulting cell suspension was then mixed with 100ul of pHrodo-green labeled myelin (50ug/ml in DPBS+0.5%BSA) or FAM-Abeta (200 nM in DPBS + 0.5% BSA) and incubated at 37°C for 45min with occasional gentle mixing. Cell suspensions were then washed and stained with the following antibodies in FACS buffer (1% fatty acid-free BSA and 1mM EDTA in PBS) for 25 minutes on ice: CD11b-BV421 (BioLegend, 101251) and Mouse Fc blocker (anti-mouse CD16/32, BioLegend, 101320). Cells were washed with FACS buffer, resuspended in FACS buffer with Propidium Iodide (Miltenyi, 130-93-233) and strained through a 100 µm filter before flow cytometry analysis on a BD FACS ARIA III. The percentage of myelin positive microglia (pHrodo-green+, CD11b+) and Abeta positive microglia (FAM+, CD11b+) in the total CD11b+ microglial population was calculated.

Instrument	BD FACSCanto II and BD FACS ARIA III, San Jose, CA
Software	FlowJo
Cell population abundance	Cell populations evaluated are not rare
Gating strategy	Single cells were separated from debris by FSC and SSC characteristics. Live microglia were identified as a population of CD11b+ and Propidium Iodide-low cells. pHrodo-myelin or FAM-Abeta uptake was then quantified in 20,000 microglia recorded from each sample.

☒ Tick this box to confirm that a figure exemplifying the gating strategy is provided in the Supplementary Information.